ACS Catalysis

Research Article

pubs.acs.org/acscatalysis

Mechanistic Details and Reactivity Descriptors in Oxidation and Acid Catalysis of Methanol

Prashant Deshlahra,[†] Robert T. Carr,[†] Song-Hai Chai,[†] and Enrique Iglesia*[,†,‡]

[†]Department of Chemical Engineering, University of California at Berkeley and [‡]Chemical Sciences Division, E.O. Lawrence Berkeley National Laboratory Berkeley, Berkeley, California 94720, United States

Supporting Information

ABSTRACT: Acid and redox reaction rates of CH_3OH-O_2 mixtures on polyoxometalate (POM) clusters, together with isotopic, spectroscopic, and theoretical assessments of catalyst properties and reaction pathways, were used to define rigorous descriptors of reactivity and to probe the compositional effects for oxidative dehydrogenation (ODH) and dehydration reactions. ^{31}P-MAS NMR, transmission electron microscopy and titrations of protons with di-*tert*-butylpyridine during catalysis showed that POM clusters retained their Keggin structure upon dispersion on SiO_2 and after use in CH_3OH reactions. The effects of CH_3OH and O_2 pressures and of D-substitution on ODH rates show that C−H activation in molecularly adsorbed CH_3OH is the sole kinetically relevant step and leads to reduced centers as intermediates present at low coverages; their concentrations, measured from UV−vis spectra obtained during catalysis, are consistent with the effects of CH_3OH/O_2 ratios predicted from the elementary steps proposed. First-order ODH rate constants depend strongly on the addenda atoms (Mo vs W) but weakly on the central atom (P vs Si) in POM clusters, because C−H activation steps inject electrons into the lowest unoccupied molecular orbitals (LUMO) of the clusters, which are the d-orbitals at Mo^{6+} and W^{6+} centers. H-atom addition energies (HAE) at O-atoms in POM clusters represent the relevant theoretical probe of the LUMO energies and of ODH reactivity. The calculated energies of ODH transition states at each O-atom depend linearly on their HAE values with slopes near unity, as predicted for late transition states in which electron transfer and C−H cleavage are essentially complete. HAE values averaged over all accessible O-atoms in POM clusters provide the appropriate reactivity descriptor for oxides whose known structures allow accurate HAE calculations. CH_3OH dehydration proceeds via parallel pathways mediated by late carbenium-ion transition states; effects of composition on dehydration reactivity reflect changes in charge reorganizations and electrostatic forces that stabilize protons at Brønsted acid sites.

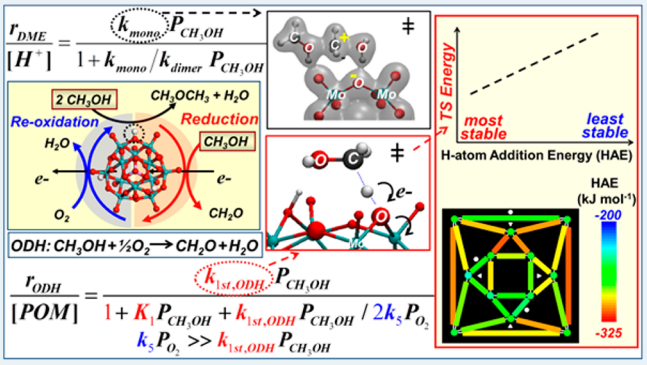

KEYWORDS: *redox cycle, C−H activation, electron transfer, in situ UV−vis spectroscopy, time-dependent DFT, H-atom addition energy*

1. INTRODUCTION

Keggin-type polyoxometalate clusters (POM; $H_nXM_{12}O_{40}$) contain Brønsted acid and redox functions and represent catalytic materials with well-defined structures that remain unchanged over a broad compositional range.[1−5] As a result, these materials are well-suited to assess reaction mechanisms and the effects of composition on catalytic reactivity and selectivity. Tungsten-based POM clusters were previously used to show how central atoms (X = P, Si, Al, Co) influence acid strength and how the latter, in turn, determines alkanol dehydration and alkene isomerization turnover rates.[6−10] Kinetic and isotopic experiments and density functional theory (DFT) showed that such reactions are mediated by ion-pair transition states; their stabilities depend on the POM deprotonation energies (DPE), on the protonation energies required to form gaseous analogues of transition states from specific reactants, on the adsorption energies for the relevant intermediates involved, and on the electrostatic interactions between the deprotonated anionic POM clusters and the cationic species at the ion-pair transition state that mediates the kinetically relevant step.[7,9,10] These rigorous connections between catalytic reactivity and the properties of catalysts and reactants enable the specific prediction and the ultimate design of catalytic properties but require mechanistic interpretations of rate data in terms of the dynamics and thermodynamics of elementary steps on well-defined structures. It is only for well-defined, but compositionally diverse, structures that theory and experiment can be combined without the ambiguities brought forth by the nonuniform and imprecise structures of most inorganic solids used as redox and acid catalysts.

Received: October 15, 2014
Revised: November 30, 2014
Published: December 24, 2014

DOI: 10.1021/cs501599y
ACS Catal. 2015, 5, 666−682

POM clusters with Mo addenda atoms and charge-balancing protons catalyze reactions that require acid and redox functions, whether they act independently or in concert. Their known structure and compositional diversity make them ideal to probe the mechanisms of such reactions and the catalytic consequences of composition on redox processes that do not occur at detectable rates on the previously examined W-based POM clusters.[10] CH_3OH dehydration to dimethyl ether (DME) and its oxidation to formaldehyde (HCHO) and subsequent conversion to methyl formate (MF) and dimethoxymethane (DMM) probe the reactivity of these materials in these parallel bifunctional pathways[11] (Scheme 1). Selectivities and turnover rates for the

Scheme 1. Primary and Secondary Reactions of CH_3OH-O_2 Mixtures via Bifunctional Pathways Catalyzed by Acid (H^+) and Redox (O*) Sites

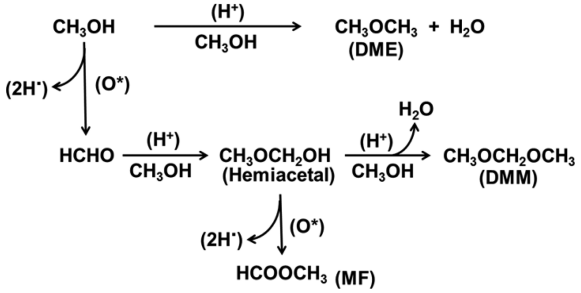

formation of primary products (DME and HCHO) have been used as functional proxies of acid and redox properties of solids.[11] The development of more rigorous composition-function relations requires, however, mechanism-based inferences of kinetic and thermodynamic constants and their rigorous connections to the properties of the solid substrate through theory and experiment, using formalisms recently applied to monofunctional Brønsted acids.[7,9,10]

Here, we provide mechanistic interpretations of CH_3OH dehydration and oxidative dehydrogenation (ODH) turnover rates on Keggin POM clusters with Mo or W addenda atoms ($H_3PMo_{12}O_{40}$, $H_4SiMo_{12}O_{40}$, $H_3PW_{12}O_{40}$). We also describe the theoretical and spectroscopic evidence for such interpretations and how they provide a rigorous demonstration of the appropriate descriptors of reactivity. Kinetic, isotopic, and UV−vis spectral data are consistent with direct DME formation via concerted reactions between coadsorbed CH_3OH molecules[10] and with Mars−van Krevelen ODH redox cycles[11−13] that kinetically couple oxidation and reduction elementary steps. The dynamics of the reduction step that limits ODH rates reflect the stability of a concerted addition of an electron to the lowest unoccupied orbitals (LUMO) in the POM clusters, located at the addenda atoms, and of a proton to an O-atom in the POM clusters in an H-abstraction step mediated by a late transition state (TS). As a result, the TS energy strongly correlates with the energy involved in adding an H-atom to the O-atom that stabilizes the transition state (or H-atom addition energy; HAE). HAE values vary significantly with the location of the abstracting O-atom within the POM cluster of a given composition, thus requiring that HAE values be rigorously averaged over all O-atoms to describe measured ODH turnover rates on clusters with different compositions.

2. METHODS

2.1. Preparation and Structural Characterization of Supported POM Clusters. SiO_2 (Cab-O-Sil, 304 $m^2\ g^{-1}$, 1.5 $cm^3\ g^{-1}$ pore volume) was washed three times with 1 M HNO_3 (10 $cm^3\ (g\text{-}SiO_2)^{-1}$) and treated in flowing dry air (UHP Praxair, 0.83 $cm^3\ g^{-1}\ s^{-1}$) overnight at 383 K. These SiO_2 samples were then treated in flowing dry air (UHP Praxair, 0.5 $cm^3\ g^{-1}\ s^{-1}$) at 573 K for 5 h before incipient wetness impregnation with solutions of $H_3PMo_{12}O_{40}$ (H_3PMo, 99.99%, Sigma-Aldrich) in double-distilled and deionized water (1.5 cm^3 solution per g dry SiO_2) at ambient temperature. Impregnated samples were kept in closed vials at ambient temperature for 24 h and then treated in flowing He (99.999%, Praxair, 0.83 $cm^3\ g^{-1}\ s^{-1}$) at 323 K for 24 h. All samples were pressed into wafers, crushed, and sieved to retain 106−180 μm aggregates. POM surface densities were set by the POM concentration in the impregnating solutions (0.030−0.76 g POM cm^{-3}) and ranged from 0.04 to 0.7 POM nm^{-2}, which correspond to 0.05 to 0.8 theoretical monolayers (1 ML = 0.88 POM nm^{-2}, using 1.2 nm for the van der Waals POM diameter[14]). Samples are denoted as $H_3PMo/SiO_2(\varphi)$, where φ denotes the POM surface density (in units of POM nm^{-2}). $H_4SiMo_{12}O_{40}$ (99.99%, Sigma-Aldrich) was dispersed on SiO_2 at a surface density of 0.16 POM nm^{-2} (0.18 ML) using the same protocols.

Solid-state ^{31}P nuclear magnetic resonance spectra were measured for unsupported and supported $H_3PMo_{12}O_{40}$ under magic-angle spinning (^{31}P-MAS NMR). A Bruker DSX-500 spectrometer (11.7 T and 202 MHz for ^{31}P) or a 300 MHz spectrometer with Techmag discovery console (7.0 T and 121 MHz) were employed along with a 4 mm Bruker CPMAS probe, and a zirconia rotor; the samples were spun at 8 kHz. Radio frequency pulses (4 μs, 90 deg) were used with ^1H decoupling pulses and delay times of 100 and 20 s for bulk and supported samples, respectively. All chemical shifts were referenced to 85 wt % H_3PO_4 solutions.

Bright-field transmission electron microscopy (TEM) images were acquired using a FEI Tecnai 12 transmission electron microscope (120 kV accelerating voltage) and an internal charge-coupled device (CCD) camera. Samples were ground into fine powders with a mortar and pestle, suspended in chloroform (99.9%, Fisher Scientific, 10 mg in 10 cm^3 chloroform), and deposited onto an ultrathin carbon film supported on a copper grid (400 mesh, Ted Pella Inc.).

2.2. Rate and Selectivity Measurements with CH_3OH-O_2 Reactants. CH_3OH conversion rates and selectivities were measured on SiO_2-supported POM catalysts (0.01−0.1 g, 106−180 μm aggregates) at 433 K using a tubular quartz reactor with plug-flow hydrodynamics. The temperature was set using a resistively heated furnace and a temperature controller (Watlow, Series 988) and was measured with a thermocouple (Omega, K-type) located in a dimple on the reactor wall. Samples were treated in 20 kPa O_2 (99.999%, Praxair, 0.5 $cm^3\ s^{-1}$) with 2.7 kPa H_2O (distilled and deionized; "wet" pretreatment) or without H_2O ("dry" pretreatment) by increasing the temperature at 0.05 K s^{-1} to 433 K and holding for 0.5 h before exposing samples to reactants.

Reactant mixtures contained CH_3OH (99.9%, Fisher Scientific), O_2 (99.999%, Praxair), He (99.999%, Praxair), and H_2O (doubly distilled and deionized). CH_3OH and H_2O were evaporated into flowing O_2/He streams at 393 K using liquid syringe pumps (Cole Parmer, 60061 Series). He and O_2 were metered using mass flow controllers (Porter Instrument) at flow

DOI: 10.1021/cs501599y
ACS Catal. 2015, 5, 666−682

rates that were adjusted to give the desired CH_3OH and O_2 pressures (0.15−4 kPa and 0.3−80 kPa, respectively) and residence times (5−60 POM s CH_3OH^{-1}). CH_3OH conversions were kept below 20%. All transfer lines after liquid injection were kept above 393 K to prevent condensation of reactants and products.

Reactant and product concentrations were measured by gas chromatography (Agilent 6890) using a methyl silicone capillary column (HP-1, 25 m × 0.32 mm × 1.05 μm) connected to a flame ionization detector and a Porapak Q packed column (80−100 mesh, 12 ft. × 1/8 in.) connected to a thermal conductivity detector. Dimethyl ether (DME), formaldehyde (HCHO), methyl formate (MF), dimethoxymethane (DMM), and H_2O were the only products detected. CO and CO_2 were not detected in the reactor effluent. Methanol ODH rates (r_{ODH}; normalized per POM cluster) are defined as the sum of HCHO, MF and DMM molar formation rates ($r_{ODH} = r_{HCHO} + r_{MF} + r_{DMM}$) because each of these products requires the initial oxidation of one CH_3OH molecule to HCHO (Scheme 1).[11] DME ODH rates were much lower than CH_3OH ODH rates on Mo Keggin POM[15] and MoO_3 domains;[16] thus, secondary reactions of DME formed by CH_3OH dehydration did not contribute to the products detected during CH_3OH-O_2 reactions.

The experimental methods described above were also used to perform reactions, measure effluent concentrations, and calculate rates with isotopically unlabeled and labeled CH_3OH (99.9%, Fisher Scientific), CH_3OD (99.5%, Alfa Aesar), and CD_3OD (99.8%, Alfa Aesar) as reactants on H_3PMo/SiO_2(0.16). The kinetic isotope effects derived from these measurements were used to confirm the kinetic relevance of elementary steps involving CH or OH bond activation inferred from measured rate equations and energy calculations using theory.

DME formation and ODH reactions both produce H_2O (Scheme 1), which inhibits ODH reactions by competing with CH_3OH for redox sites. The conversions achieved in some of these kinetic experiments (up to 20%) deplete reactants slightly along the catalyst bed. As a result, rate and equilibrium constants for ODH and DME formation were obtained by regressing rate data using the integral form of their respective rate equations (regression details in Supporting Information (SI)), thus rigorously accounting for these concentration gradients along the catalyst bed. The rates reported in Sections 3.3 and 3.5 were extrapolated to zero conversion using the integrated form of these rate equations and the regressed rate and equilibrium constants (details in SI). These extrapolated values reflect rates of formation of primary products at the conditions of the reactor inlet, and restrict the kinetic effects of H_2O to those intended by the purposeful addition of H_2O to the CH_3OH-O_2 reactants.

2.3. Titration of Brønsted Acid Sites during CH_3OH-O_2 Reactions. Brønsted acid sites on supported POM clusters were titrated during reactions of CH_3OH-O_2 mixtures at 433 K by introducing 2,6-di-*tert*-butylpyridine (DTBP, > 97%, Aldrich) dissolved in CH_3OH or CH_3OH-H_2O mixtures into flowing O_2/He mixtures (both 99.999%, Praxair) to give the target CH_3OH, H_2O, O_2, and DTBP (7 Pa) pressures. Samples were treated using the procedures described in Section 2.2 before introducing reactants and titrants. The amount of adsorbed DTBP was calculated from its residual concentration in the effluent stream using the chromatographic protocols described in Section 2.2. Saturation titrant uptakes were defined as those required to fully suppress CH_3OH dehydration rates. Large DTBP molecules at protons can potentially block neighboring redox sites causing inhibition of ODH rates; such steric occlusion was probed by comparing titrant uptakes using a titrant with smaller size (dimethylethyl amine, 99%, Aldrich, 12 Pa).

2.4. UV−vis Spectroscopy during CH_3OH-O_2 Reactions. UV−vis spectra were measured using a Varian-Cary 6000i spectrometer equipped with a Harrick Scientific diffuse reflectance attachment (DRP-XXX) and a reaction chamber (DRA-2CR) modified by placing a stainless steel frit at the bottom of sample cup to minimize thermal gradients and to ensure uniform reactant flow through the packed powder samples. The temperature was set using a heating element located below the sample holder and a temperature controller (Watlow, Series 982) and was measured with a K-type thermocouple (Omega) located at the sample holder wall. All UV−vis spectra were acquired using ~0.01 g catalyst (aggregates smaller than 106 μm) and a constant inlet flow rate (2.0 cm^3 s^{-1}).

Reactant mixtures contained CH_3OH (99.9%, Fisher Scientific), O_2 (99.999%, Praxair), He (99.999%, Praxair), and H_2O (deionized). CH_3OH and H_2O were evaporated into flowing O_2/He streams at 433 K using a liquid syringe pump (Cole Parmer, 60061 Series). He and O_2 were metered using mass flow controllers (Porter Instrument) at flow rates adjusted to give the target CH_3OH and O_2 pressures. Catalysts were treated in 80 kPa O_2 during temperature ramping (0.083 K s^{-1}) and for 0.5 h at reaction temperature before introducing reactants. Spectra were collected between 0.7 and 6.0 eV at a scanning rate of 10 nm s^{-1} before and during CH_3OH-O_2 reactions (433 K, 0.25−1 kPa CH_3OH, 2−80 kPa O_2, 0−2.25 kPa H_2O). Steady-state pre-edge intensities at given CH_3OH and H_2O pressures were measured (at a fixed energy of 1.8 eV) 3 h after the first introduction of CH_3OH-O_2-H_2O mixtures and 0.5 h after each change in O_2 pressure in order to reach steady-state. The Kubelka−Munk function, $F(R_\infty)$ ($R_\infty = R_{sample}/R_{reference}$) was used to convert reflectance data into absorption spectra[17,18] using MgO as the reference reflector according to:

$$F(R_\infty) = \frac{(1 - R_\infty)^2}{2R_\infty} = \frac{K}{S} \quad (1)$$

where K and S reflect the absorption and scattering coefficients of the sample, respectively. Edge energies of the absorption band in the spectra were measured from the intercept of the near-edge region when $[F(R_\infty)h\nu]^{1/2}$ was plotted as a function of $h\nu$,[19] where h and ν are Planck's constant and frequency of UV−vis radiation, respectively.

2.5. Computational Methods. Periodic density functional theory (DFT) calculations were performed using the Vienna ab initio Simulation Package (VASP).[20] Exchange and correlation energies were calculated using the Perdew−Wang (PW91) functional within the generalized-gradient approximation.[21] The valence electron wave functions were represented by a periodic plane-wave basis-set expansion to a cutoff energy of 400 eV; the interaction between valence and core electrons was described using the projector augmented wave (PAW) method.[22] Electronic structures were converged self-consistently to energies $<1 \times 10^{-6}$ eV. Calculations were performed by specifying integer band occupancies because POM clusters are nonperiodic molecular systems. The lowest energy electronic structures of intermediates and transition states were obtained by comparing spin-restricted singlet and spin-polarized singlet, doublet or triplet electronic structure calculations, as described in detail elsewhere.[23]

DOI: 10.1021/cs501599y
ACS Catal. 2015, 5, 666−682

Full Keggin clusters (~1.2 nm diameter), gaseous H-atoms, CH_3OH molecules, and polyhedral oligomeric silsesquioxane (POSS; $Si_8O_{20}H_8$) clusters (used to model silanol groups in the silica support) were calculated by placing them at the center of a cubic unit cell with an edge-length of 2 nm to provide a vacuum region sufficiently large to prevent interactions among clusters in adjacent unit cells. Structures formed via condensation of OH groups in a POM cluster with those in another POM or a POSS cluster to release H_2O, and the uncondensed reference states for such events were calculated using unit cells with edge-lengths of 3 nm. A 1 × 1 × 1 Monkhorst−Pack k-point mesh was used to sample the Brillouin zone. The structures of all stable intermediates were optimized until forces on atoms were <0.05 eV A^{-1}. Dipole and quadrupole moments, calculated with the center of the unit cell taken as the center of charge, were used to correct for long-range interactions among neighboring unit cells. Transition-state calculations for CH_3OH ODH reactions[23] using computational details identical to this study, and for DME formation reactions[24] using nearly identical details, but with ultrasoft pseudopotentials (USPP)[25] instead of the PAW method[22] to describe electron−core interactions, are described elsewhere.[23,24]

Localized basis-set DFT and time-dependent DFT (TD-DFT)[26] calculations were performed using the Gaussian program[27] to obtain electronic (UV−vis) spectra of oxidized and reduced POM clusters and to compare reaction energies with those obtained from periodic plane-wave calculations. Hybrid-DFT functionals (B3LYP[28]) and double-ζ basis sets (Aug-cc−PVDZ-PP with core potentials for Mo and 6-31G(d,p) for H, C, O, and P atoms) were used for ground-state geometry optimization as well as for excited states calculation using TD-DFT. The ground-state energies and forces on atoms were converged to $<1 \times 10^{-6}$ Ha and $<4.5 \times 10^{-3}$ Ha/bohr, respectively. Excited states were calculated from 1200 initial guesses with retention of the 300 excited states with the lowest energies (converged to $<1 \times 10^{-4}$ eV). The UV−vis spectra were obtained from calculated excitation energies and oscillator strengths by broadening all excitation delta-functions as Gaussian functions of width 0.15 eV and summing over the Gaussian functions.

3. RESULTS AND DISCUSSION

3.1. Structural and Surface Properties of SiO_2-Supported POM Clusters. Figure 1 shows solid-state ^{31}P-MAS NMR spectra (ref 85% H_3PO_4 aq.) for unsupported $H_3PMo_{12}O_{40}$ clusters and for supported $H_3PMo/SiO_2(0.16)$ samples before and after reactions of CH_3OH-O_2 or CH_3OH-O_2-H_2O mixtures (2 h at 433 K in 4 kPa CH_3OH, 20 kPa O_2, 0 or 2.7 kPa H_2O); the expected chemical shifts for different species and lacunary structures, identified in the aqueous synthesis mixtures of POM clusters,[29] are also shown (dotted vertical lines in Figure 1). The unsupported POM sample showed a peak at −3.6 ppm (with a shoulder at −3.9 ppm) while $H_3PMo/SiO_2(0.16)$ showed a slight shift downfield from the unsupported sample before (−3.2 ppm) and after (−3.3 ppm) reaction in CH_3OH-O_2-H_2O, and a further shift (−2.7 ppm) with some broadening after CH_3OH-O_2 reactions without added H_2O.

The observed ^{31}P NMR lines (Figure 1) are within the range of the chemical shifts reported in the literature for solid and solvated intact Keggin ($H_xPMo_{12}O_{40}^{3-x}$, −3.9 to −2.7 ppm[2,29,30]) or Wells−Dawson ($H_xP_2Mo_{18}O_{60}^{6-x}$, −3.4 to −2.2 ppm[2,29,30]) clusters; no spectral features for lacunary structures,[29] formed via partial decomposition of POM clusters, were detected (dotted vertical lines in Figure 1). The presence of Wells−Dawson structures is unlikely, as they are less thermally stable than Keggin clusters[30] and known to form via dimerization of PMo_9O_{31} lacunary structures[29] that are absent from all spectra. Thus, we conclude that supported clusters have intact Keggin structure after exposure to reactants at reaction conditions. Such conclusions are expected to extend to clusters with Si central atoms but could not be confirmed because H_4SiMo samples contain NMR-inactive ^{28}Si, and any signal from trace amounts of ^{29}Si nuclei, if measurable, would be overwhelmed by the trace ^{29}Si NMR signal from the SiO_2 support.

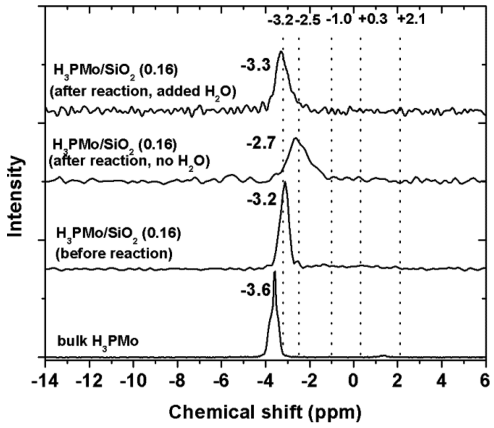

Figure 1. Solid-state ^{31}P-MAS NMR spectra of unsupported H_3PMo and $H_3PMo/SiO_2(0.16)$ before reaction, and $H_3PMo/SiO_2(0.16)$ after 2 h of CH_3OH-O_2 catalysis without and with H_2O added to reactants (433 K, 4 kPa CH_3OH, 20 kPa O_2, 0 or 2.7 kPa H_2O). Dotted vertical lines at −3.2, −2.5, −1, +0.3, and +2.1 ppm reflect average chemical shifts of $H_xPMo_{12}O_{40}^{-3+x}$ Keggin anions, $H_xP_2Mo_{18}O_{62}^{-6+x}$ Wells−Dawson anions, and PMo_{11}, PMo_9, and P_2Mo_5 lacunary structures, respectively, as identified in aqueous POM synthesis mixtures.[29] All shifts are referenced to 85% H_3PO_4 (aq.).

The slight downfield shift in the NMR lines for H_3PMo clusters on SiO_2 relative to crystalline POM structures (Figure 1) may reflect the loss of water of crystallization from the bulk $H_3PMo_{12}O_{40}{\cdot}xH_2O$ crystals, leading to hydrated protons ($[H_2O{-}H{-}OH_2]+$) being replaced by covalent O−H bonds,[2] or the partial dehydroxylation of POM clusters via condensation of their O−H groups with silanols.[31] The reported effects of the loss of H_2O[2] are consistent with the direction of shifts observed in NMR lines and with the smaller extents of the shifts when H_2O is added to CH_3OH-O_2 reactants (Figure 1).

The effects of H_2O on the NMR spectra of POM clusters were probed by comparing DFT-derived P−O bond-lengths with reported chemical shifts for several PO_4^{3-}-containing species[2] (SI, Figure S2). These comparisons indicate that ^{31}P NMR lines shift downfield for species with longer P−O bonds, because P−O distances affect the shielding of ^{31}P nuclei by electrons.[32] DFT-derived P−O bond lengths in $H_3PMo_{12}O_{40}{\cdot}6H_2O$ increase (and approach those in H_3PO_4 molecules) when H_2O molecules are removed or POM protons condense with silanols (modeled as polyhedral oligomeric silsesquioxane clusters, POSS; Figure S2), consistent with the spectral shifts observed after catalytic reactions (Figure 1). These results are consistent with the removal of some protons during catalysis (at 433 K), possibly by intercluster or cluster-silanol dehydroxylation, which do not influence the atomic connectivity within the Keggin structure.

Figure 2 shows transmission electron micrographs for H_3PMo/SiO_2 samples with 0.04, 0.16, and 0.70 POM nm^{-2}

DOI: 10.1021/cs501599y
ACS Catal. 2015, 5, 666−682

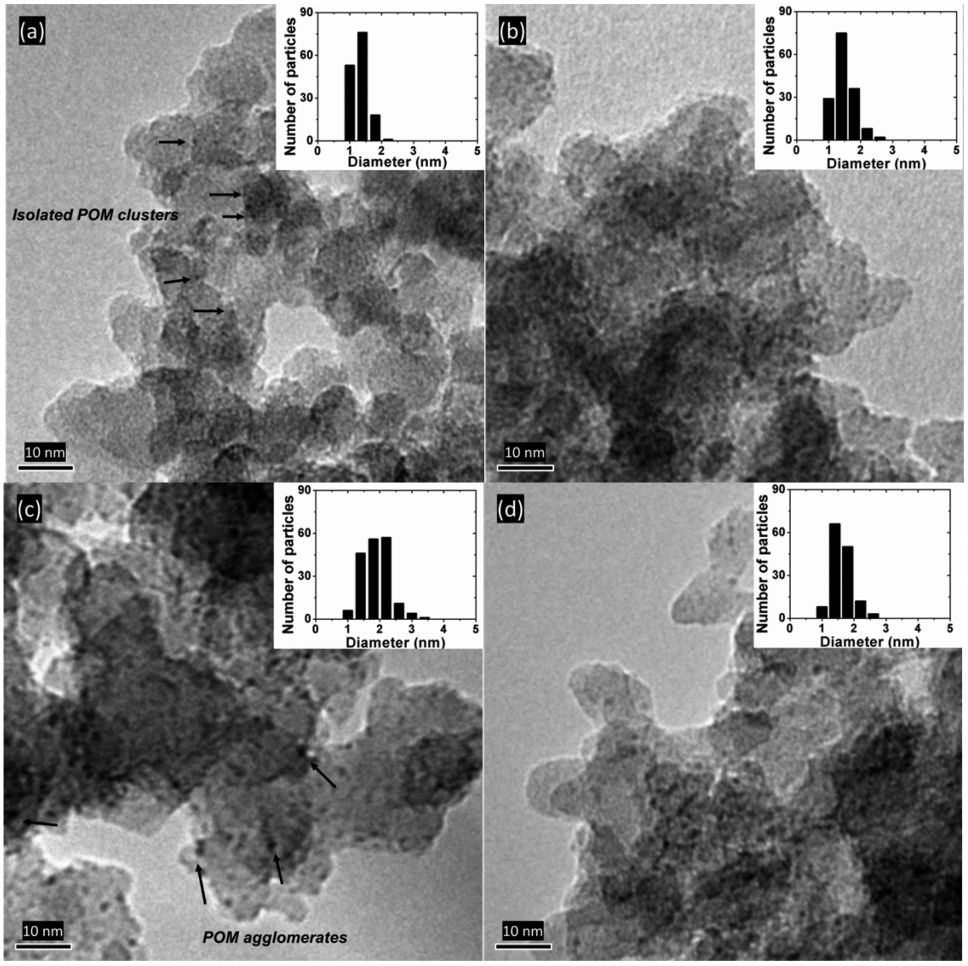

Figure 2. Transmission electron micrographs of H_3PMo/SiO_2 samples with (a) 0.04 POM nm^{-2} (148 particles; mean diameter, <*d*> = 1.3 nm), (b) 0.16 POM nm^{-2} (150 particles; <*d*> = 1.5 nm), and (c) 0.70 POM nm^{-2} (181 particles; <*d*> = 1.9 nm) surface densities. Also shown is (d) the 0.16 POM nm^{-2} sample after 2 h of CH_3OH-O_2 catalytic reaction (433 K, 4 kPa CH_3OH, 20 kPa O_2) (169 particles, <*d*> = 1.6 nm). Features corresponding to POM structures are indicated in (a) and (c).

surface densities before catalytic experiments and, for one sample (0.16 POM nm^{-2}), after CH_3OH-O_2 reactions. The small dark features in these images correspond to $H_3PMo_{12}O_{40}$ clusters (some labeled in Figure 2a,c). Their mean diameters (1.3−1.5 nm for the 0.04 and 0.16 POM nm^{-2} samples; Figure 2a,b) are similar to the van der Waals diameter of $H_3PMo_{12}O_{40}$ clusters (1.2 nm from X-ray diffraction[14]). These images indicate that POM clusters remain essentially isolated at these surface densities, with only a small fraction present as aggregates; small POM aggregates become evident at higher POM surface densities (0.7 POM nm^{-2} mean diameter 1.9 nm, Figure 2c) but remain two-dimensional in structure throughout the range of surface densities examined. These TEM images also show that reactions of CH_3OH (2 h at 433 K, 4 kPa CH_3OH, 20 kPa O_2) led to slightly larger TEM features (from 1.5 to 1.6 nm; Figure 2d).

The effects of POM surface density (0.04 to 0.7 POM nm^{-2}) and CH_3OH reaction conditions on the number of accessible protons were probed by titrating H_3PMo/SiO_2 (0.04 to 0.7 POM nm^{-2}) and H_4SiMo/SiO_2 (0.16 POM nm^{-2}) samples with DTBP during reactions of CH_3OH-O_2 and CH_3OH-O_2-H_2O mixtures (433 K, 4 kPa CH_3OH, 20 kPa O_2, 0 or 2.7 kPa H_2O; Figure 3). DTBP forms protonated structures that bind irreversibly, thus rendering Brønsted acid sites inaccessible for catalysis; these molecules cannot coordinate to Lewis acid sites,

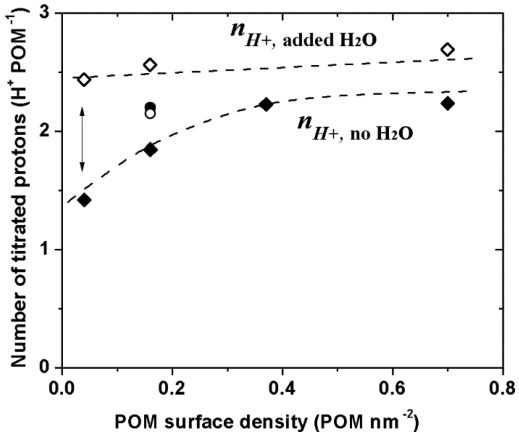

Figure 3. Number of protons titrated by 2,6-di-*tert*-butylpyridine on H_3PMo/SiO_2 (♦, ◇) and H_4SiMo/SiO_2 (●, ○) catalysts, during reactions in CH_3OH-O_2 (closed symbols) and CH_3OH-O_2-H_2O (open symbols) mixtures, as a function of POM surface density (433 K, 4 kPa CH_3OH, 20 kPa O_2, 7 Pa DTBP, 0 or 2.7 kPa H_2O). Dashed curves represent qualitative trends.

because access to the N-atom is hindered by the vicinal *tert*-butyl groups.[33]

DOI: 10.1021/cs501599y
ACS Catal. 2015, 5, 666−682

DTBP uptakes per H_3PMo cluster during CH_3OH-O_2 reactions were smaller than the stoichiometric number of protons (3.0 H^+ POM^{-1}) and increased monotonically with increasing surface density (1.4 to 2.2 DTBP POM^{-1} for 0.04 to 0.70 POM nm^{-2}; Figure 3). Uptakes approached stoichiometric values and became less sensitive to POM surface density when CH_3OH-O_2 reactions were carried out with added H_2O (2.4 to 2.7 DTBP POM^{-1} for 0.04 to 0.70 POM nm^{-2}; Figure 3). The smaller and substoichiometric numbers of protons in the absence of added water may reflect (i) the formation of secondary POM structures with inaccessible interstitial protons or (ii) the loss of protons (as H_2O) via intracluster or intercluster dehydroxylation[15,34] or via condensation with silanols.[31] The larger uptakes on the H_3PMo/SiO_2 samples with higher surface density, for which some agglomeration was evident in TEM images (Figure 2), and the reported ability of polar CH_3OH molecules to swell the interstices among POM clusters in secondary structures[35] suggest that cluster dehydroxylation via condensation with silanols is responsible for the substoichiometric DTBP uptakes.

The thermodynamics of such dehydroxylation events were explored by comparing the DFT derived energies of isolated intact Keggin clusters to their dehydroxylated forms (results in SI; Figure S4, Table S1). The calculated energies reflect enthalpies at 0 K (uncorrected by zero-point vibrational energies), used to estimate relative difference among different types of dehydroxylations. The free energies at relevant temperature and reactant pressures are, however, expected to be lower than these values, due to the entropy gained by the release of gaseous H_2O. Dehydroxylation of POM clusters via condensation with silanols (modeled as O−H groups at polyhedral oligomeric silsesquioxane, POSS; Figure S4) was found to be much less endothermic (ΔE = +28 kJ mol^{-1}; Table S1) than intercluster or intracluster dehydroxylations (ΔE = +80 and +134 kJ mol^{-1}, respectively; Table S1).

Thus, we conclude that the incipient formation of secondary POM structures serves to protect the interstitial protons from contact with silanols, while H_2O, when added to the reactants, decreases the thermodynamic tendency for dehydroxylation via condensation with silanols (or other POM clusters), which causes larger DTBP uptakes per POM (Figure 3). DTBP uptakes on H_4SiMo/SiO_2(0.16) were similar in CH_3OH-O_2 and CH_3OH-O_2-H_2O reactants (2.2 DTBP POM^{-1}; Figure 3), but also were a smaller fraction of the stoichiometric number (4 DTBP POM^{-1}) of protons than for H_3PMo/SiO_2 samples. These uptakes suggest that H_4SiMo clusters may have a greater thermodynamic tendency for dehydroxylation, thus making such processes less reversible upon contact with H_2O addition. Taken together, these data and theoretical treatments indicate that the synthetic protocols used here form POM clusters with intact Keggin structures that are accessible to reactants at low surface densities (<0.16 POM nm^{-2}).

3.2. Site Requirements for DME Formation and ODH Reactions. In this section, we probe the bifunctional properties of Mo-based POM clusters via acid and oxidation reactions of CH_3OH. Figure 4 shows ODH and DME formation rates (per POM) from CH_3OH-O_2 reactants on H_3PMo/SiO_2(0.16) before and during titration with DTBP (433 K, 4 kPa CH_3OH, 20 kPa O_2, 7 Pa DTBP), measured using procedures described in sections 2.2 and 2.3. Both rates decreased monotonically with increasing DTBP uptakes; saturation uptakes fully suppressed DME formation and led to a marked decrease in ODH rates (~20% of initial rates at saturation; Figure 4). Similar trends were

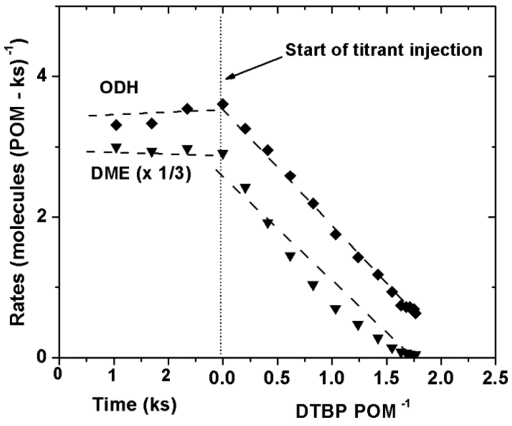

Figure 4. Titration of H_3PMo/SiO_2(0.16) with 2,6-di-*tert*-butylpyridine (DTBP) during CH_3OH-O_2 catalysis. CH_3OH ODH (♦) and DME formation (▼) rates are shown as a function of reaction time and of the cumulative amount of titrant adsorbed (433 K, 4 kPa CH_3OH, 20 kPa O_2, 7 Pa DTBP, 0 kPa H_2O).

observed on H_3PMo/SiO_2 samples with 0.04 to 0.70 POM nm^{-2} surface densities and on H_4SiMo/SiO_2 (0.16 POM nm^{-2}) for titrations in the presence of CH_3OH-O_2 with or without added H_2O.

These data suggest that DME forms exclusively at Brønsted acid sites and DTBP-uptakes can be used to normalize measured rates to determine DME formation turnover rates, thus allowing assessments of intrinsic reactivity and accurate comparisons among different Brønsted acid catalysts. The concurrent inhibition of ODH reactions by DTBP indicates that either bulky protonated DTBP species at acid sites occlude vicinal redox-active sites or that the transfer of a proton from the POM cluster to DTBP upon binding influences the redox properties of the POM cluster. Use of a smaller titrant (dimethyl−ethyl amine, DMEA) in the titration experiments, for which steric hindrance would be much weaker, decreased ODH rates even more significantly than DTBP (Figure S5, SI; < 5% of initial rates at saturation with DMEA), suggesting that redox modifications are responsible for the effects of titrant adsorption on ODH rates. Such electronic modifications were confirmed by DFT calculations of H-atom addition energies (HAE) at O-atoms in the POM clusters. The DFT-derived reaction-averaged HAE values (obtained using procedures described in Section 3.7) became less negative when pyridine or DMEA titrated the three protons in a $H_3PMo_{12}O_{40}$ cluster (from −302 to −289 and −287 kJ $mol^{-1}$for pyridine and DMEA, respectively; Figure S7, SI). Such increase in HAE values would lead, in turn, to less stable ODH transition states (as also shown in Section 3.7) and to the observed decrease in ODH rates upon titration of protons by DTBP (Figure 4). We conclude from these experiments and calculations that DME forms directly on Brønsted acid sites and that the ODH turnovers occur at separate redox sites that are influenced by the titration of protons by bases.

DME formation rates (per POM cluster; 433 K, 4 kPa CH_3OH, 20 kPa O_2) increased slightly with increasing POM surface density (Figure 5), consistent with their higher proton densities (Figure 3), which we have proposed arises, in turn, from the incipient formation of secondary POM structures that inhibit contact with silanols. In contrast, ODH rates (per POM) decreased slightly with increasing surface density, suggesting that the extent of dehydroxylation can weakly influence the redox properties relevant for ODH reactivity. These trends indicate

DOI: 10.1021/cs501599y
ACS Catal. 2015, 5, 666−682

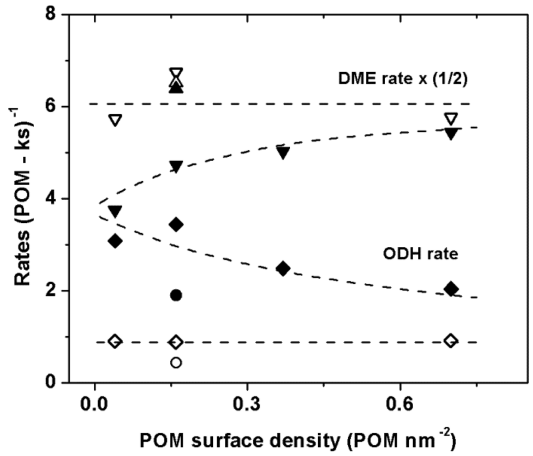

Figure 5. DME formation (▼, ▽) and CH_3OH ODH rates (♦, ◇) per POM cluster on H_3PMo/SiO_2 as a function of cluster surface density during reactions in CH_3OH-O_2 (closed symbols) and CH_3OH-O_2-H_2O (open symbols) mixtures (433 K, 4 kPa CH_3OH, 20 kPa O_2, 0 or 2.7 kPa H_2O, ~ 14−17% conversion). DME formation (▲, △) and ODH rates (●, ○) on H_4SiMo/SiO_2(0.16) at identical conditions are also shown. Dashed lines show qualitative trends for H_3PMo/SiO_2.

that DME formation rates (but not ODH rates) can be accurately normalized by the number of accessible protons.

The addition of H_2O (2.7 kPa) to CH_3OH-O_2 reactants led to a more significant increase in DME formation rates (per POM) on low surface density H_3PMo/SiO_2 samples than on samples with higher surface densities (in the range 0.04 to 0.7 POM nm^{-2}; Figure 5), consistent with the concomitant increase in the number of accessible protons (per POM; Figure 3). ODH rates (per POM) decreased upon H_2O addition, because of competitive adsorption of H_2O and CH_3OH at redox sites (Section 3.3). The effects of POM surface density on DME and ODH rates (per POM) became undetectable when H_2O was present (H_3PMo/SiO_2; Figure 5, 2.7 kPa H_2O) because clusters with different surface density, which dehydrate to different extents in the absence of H_2O, apparently achieve similar hydration levels when H_2O is present, as shown by the measured DTBP uptakes per POM (Figure 3). DME formation rates (per POM) on H_4SiMo/SiO_2 (0.16) were similar to CH_3OH-O_2 and CH_3OH-O_2-H_2O reactant mixtures (Figure 5, 2.7 kPa H_2O), consistent with the similar DTBP uptakes at both conditions (Figure 3).

The stability of H_3PMo/SiO_2 (0.16) clusters was also influenced by the H_2O pressure (SI, Figure S8). ODH rates with CH_3OH-O_2-H_2O reactants became stable after a small decrease in DME rates (<10%) and a small increase in ODH rates (<5%) over the initial 2 h. The removal of H_2O from the CH_3OH-O_2 stream did not influence DME formation rates, but immediately increased ODH rates, consistent with the kinetic nature of the inhibition by coadsorbed H_2O (section 3.3). Slow transients after H_2O removal led to a slow decrease in DME formation rates and a slow increase in ODH rates (over 3 h), in agreement with the gradual loss of some protons evident from the lower DTBP uptakes and DME rates and from the higher ODH rates in the absence of added H_2O (Figures 3, 5). Such structural changes were minimized during measurements of the kinetic effects of reactant and product concentrations on DME formation and ODH rates by maintaining the catalysts at a standard reference condition (4 kPa H_2O, 20 kPa O_2, 2.7 kPa H_2O) and returning to this condition after acquiring rate and selectivity data at each reactant and product concentration.

3.3. Elementary Steps and Effects of Reactant Pressures for CH_3OH Oxidative Dehydrogenation Rates.

Here, we examine the elementary steps involved in CH_3OH ODH on bifunctional POM clusters by deriving rate equations consistent with these sequences and interpreting the chemical origins of the measured rate constants in order to assess the effects of composition on redox properties of POM and the relevance of such properties as the descriptors of reactivity.

Scheme 2 shows a plausible sequence of elementary steps for the conversion of CH_3OH to HCHO via Mars−van Krevelen

Scheme 2. Proposed Elementary Steps for CH_3OH Oxidative Dehydrogenation (ODH) on Redox Sites of POM Clusters

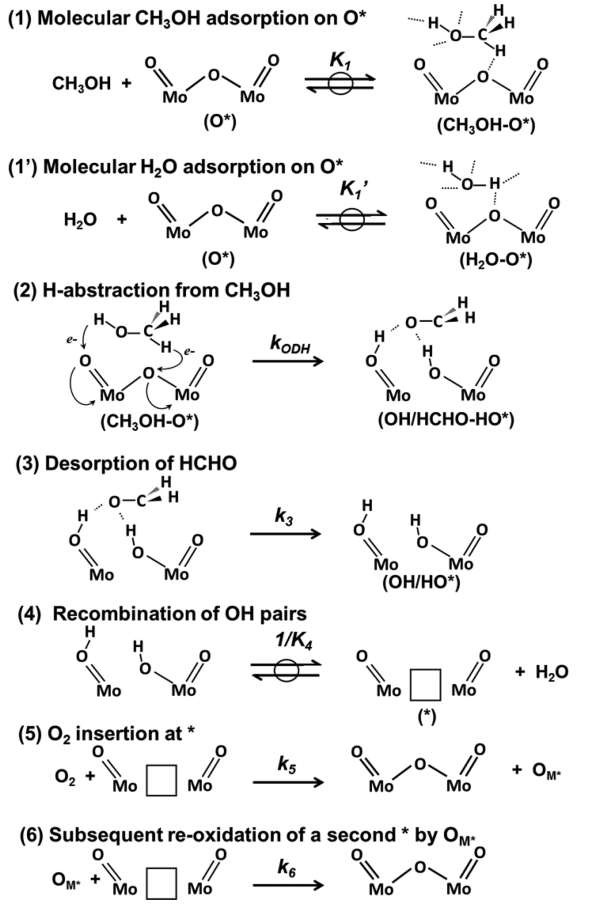

redox cycles.[13] Similar elementary steps, but mediated by methoxy species formed via CH_3OH dissociation, instead of molecular CH_3OH, have been proposed for CH_3OH and CH_3CH_2OH ODH reactions on supported MoO_x,[11,36,37] VO_x,[11,32,38] and RuO_x[39] domains and on Fe molybdates.[12] The first step involves the quasi-equilibrated adsorption of CH_3OH (CH_3OH-O*) at lattice O-atoms (O*) (Step 1, Scheme 2), previously claimed to occur dissociatively based on the observed formation of methoxy species during stoichiometric reactions of CH_3OH on metal oxides.[37] Reactivity data, however, cannot discern the molecular or dissociative nature of such steps, because both routes lead to the same rate equation.[23] DFT calculations clearly show, however, that C−H activation occurs in undissociated CH_3OH-O* using lattice oxygen atoms as the H-abstractors at all relevant reaction conditions.[23] H_2O, whether

DOI: 10.1021/cs501599y
ACS Catal. 2015, 5, 666−682

formed or added to CH_3OH-O_2 reactants, can adsorb on O* to form H_2O−O* species in quasi-equilibrated steps (Step 1′, Scheme 2).

Subsequent irreversible steps sequentially abstract H-atoms from the C and O-atoms in adsorbed methanol using vicinal O* species to form HCHO and OH pairs (OH/HCHO-HO*). Measured kinetic isotope effects and DFT estimates have shown that the H-abstraction from the C−H bond is the sole kinetically relevant step[23] and that each H-abstraction step leads to a one-electron reduction of the POM cluster (Step 2; Scheme 2). HCHO* can desorb (Step 3 in Scheme 2) or react with another CH_3OH to form hemiacetals (CH_3OCH_2OH), which undergo either condensation with another CH_3OH (to form dimethoxymethane, DMM) or H-abstraction (to form methyl formate, MF; Scheme 1). These steps determine ODH selectivity and can occur before or after desorption of the primary HCHO products, but they do not influence the value of the measured ODH rates, because each product molecule formed requires one initial ODH event. The reduced centers formed consist of vicinal OH pairs (OH/HO*), which can recombine to form gaseous H_2O and an O-vacancy (*, Step 4, Scheme 2). In the reverse of this step, H_2O readsorbs onto vacancies to form vicinal OH pairs. Gaseous O_2 ultimately reacts with two O-vacancies via sequential steps that titrate one vacancy by irreversible O_2 dissociation (Step 5 in Scheme 2) and then a second one by migration of the other O-atom (O_M*; Step 6 in Scheme 2); these latter steps remain uncertain in mechanistic details, but they are irrelevant in determining the rate of CH_3OH conversion via ODH reactions.[40]

A pseudo-steady-state analysis of surface intermediates and the assumptions of quasi-equilibrated CH_3OH and H_2O molecular adsorption and OH recombination steps and irreversible H-abstraction and O_2 activation lead to the ODH rate equation (derivation details in SI):

$$\frac{r_{ODH}}{[POM]} = \frac{k_{ODH}K_1P_{CH_3OH}}{1 + K_1P_{CH_3OH} + K_1'P_{H_2O} + \frac{k_{ODH}K_1P_{CH_3OH}}{2k_5P_{O_2}}\left(1 + K_4P_{H_2O}\right)} \quad (2)$$

(O*) (CH$_3$OH-O*) (H$_2$O-O*) (*) (OH/HO*)

in which each denominator term corresponds to the ratio of concentrations between the surface species listed in parentheses and O*. K_1 and K_1' are the equilibrium constants for molecular adsorption of CH_3OH and H_2O at O*, respectively, K_4 is the equilibrium constant for H_2O dissociation at vacancies (*) to form OH pairs, whereas k_{ODH} and k_5 are the rate constants for C−H activation and for the first step in the O-vacancy reoxidation sequence, respectively. Scheme 2 and eq 2 reflect the kinetic coupling between steps that reduce O* sites (Step 2, k_{ODH}) and those that reoxidize * sites (Step 5, k_5) on POM clusters; the resulting (O*)/(*) ratios depend on the O_2/CH_3OH reactant ratio and the kinetic relevance shifts from reduction to reoxidation steps as this ratio decreases.

The effects of CH_3OH, H_2O and O_2 pressures on measured ODH rates on H_3PMo/SiO_2(0.16) (Figures 6a, 7, and 8, respectively) and H_4SiMo/SiO_2(0.16) (SI; Figure S9) samples are consistent with the functional form of eq 2 when step 2 in Scheme 2 is the sole kinetically relevant step. The nonlinear dependence of ODH rates on CH_3OH pressure (Figure 6a) indicates that the most abundant surface intermediate (MASI) shifts from O* to CH_3OH-O* as the CH_3OH pressure increases (eq 2). O_2 pressure did not influence ODH rates in the presence or absence of added H_2O (0 or 2.7 kPa) at any O_2/CH_3OH ratio

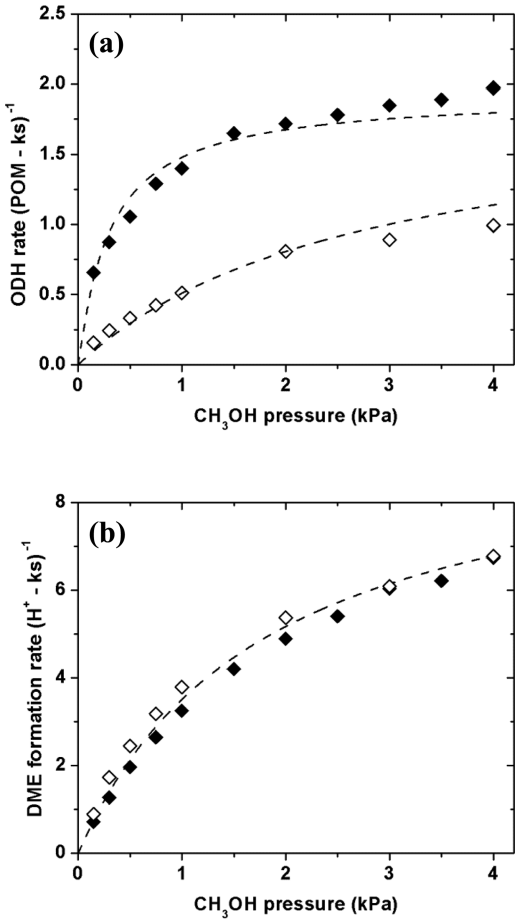

Figure 6. (a) CH_3OH ODH and (b) DME formation rates as a function of CH_3OH pressure on H_3PMo/SiO_2 (0.16) with (open symbols) and without (closed symbols) H_2O added to reactants (433 K, 20 kPa O_2, 0 or 2.7 kPa H_2O). Reported rates were extrapolated to zero conversion using integral forms of eqs 3 and 9; dashed curves represent best regression fits to the form of the equations.

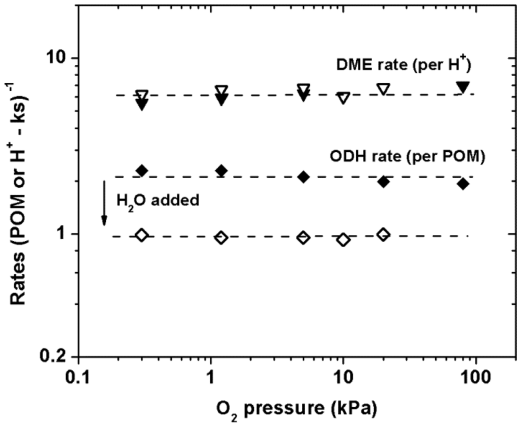

Figure 7. CH_3OH ODH (♦, ◇) and DME formation (▼, ▽) rates as a function of O_2 pressure on H_3PMo/SiO_2 (0.16) with (open symbols) and without (closed symbols) H_2O added to reactants (433 K, 4 kPa CH_3OH, 0 or 2.7 kPa H_2O). Reported rates were extrapolated to zero conversion using integral forms of eqs 3 and 9. Dashed lines represent qualitative trends.

(0.3 to 80 kPa O_2; O_2/CH_3OH 0.08 to 20; Figure 7), suggesting that fast reoxidation steps cause the reduced centers (* and OH/HO*; eq 2) to be present as minority species relative to oxidized

DOI: 10.1021/cs501599y
ACS Catal. 2015, 5, 666−682

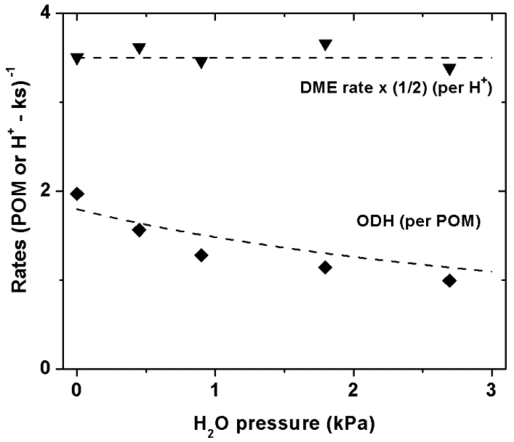

Figure 8. CH_3OH ODH (♦) and DME formation (▼) rates on H_3PMo/SiO_2 (0.16), as a function of H_2O pressure at the reactor inlet (433 K, 4 kPa CH_3OH, 20 kPa O_2). Reported rates were extrapolated to zero conversion using integral forms of eqs 3 and 9; dashed curves represent best regression fits to the form of the equations.

centers (O*, CH_3OH-O*, H_2O−O*; eq 2). As a result, the rate constant for the reoxidation steps (k_5) is absent from the rate equation and the reduction step (k_{ODH}) becomes the sole kinetically relevant step:

$$\frac{r_{ODH}}{[POM_{acc}]} = \frac{k_{ODH}K_1P_{CH_3OH}}{1 + K_1P_{CH_3OH} + K_1'P_{H_2O}} \quad (3)$$

Regression of rate data in Figure 6a to the functional form of eq 3 gives a first-order ODH rate constant ($k_{ODH}K_1$) that reflects the energy of the H-abstraction transition state ($\Delta E^{\ddagger}_{TS,ODH}$) with respect to an uncovered surface (ΔE_{O*}) and a gaseous CH_3OH molecule ($\Delta E_{CH3OH(g)}$):

$$k_{1,ODH} = k_{ODH}K_1 \sim \exp(-(\Delta E^{\ddagger}_{TS,ODH} - \Delta E_{O*} - \Delta E_{CH_3OH(g)})/RT) \quad (4)$$

and a zero-order rate constant that reflects, in turn, the energy of the same H-abstraction TS but relative to an adsorbed CH_3OH molecule ($\Delta E_{CH3OH-O*}$):

$$k_{0,ODH} = k_{ODH} \sim \exp(-(\Delta E^{\ddagger}_{TS,ODH} - \Delta E_{CH_3OH-O*})/RT) \quad (5)$$

The structure calculated using DFT, for a weakly bound molecular CH_3OH-O* species is shown in Table 1, whereas that for the kinetically relevant TS (involving C−H activation in CH_3OH-O*) is shown in Figure 9. These structures are consistent with the steps proposed in Scheme 2 and were determined by comparisons of the temperature-dependent kinetic data and isotopic experiments with the DFT-derived energies, enthalpies, and entropies for molecular and dissociative ODH routes involving CH_3OH-O* and OH/CH_3O*, respectively, as the reactive intermediates.[23] The kinetic relevance of C−H (instead of O−H) bond activation was confirmed by measuring relative ODH rates for molecules labeled with D-atoms at the C or O-atom; such measurements can discern which vibrational mode (C−H or O−H) resides along the reaction coordinate for the formation of the kinetically relevant transition state. Kinetic isotope effects (KIE), defined as the ratios of first- or zero-order rate constants regressed from rate data to the form of eq 3, were near unity for CH_3OD ($k_{ODH,CH3OH}/k_{ODH,CH3OD}$, $k_{ODH}K_{1,CH3OH}/k_{ODH}K_{1,CH3OD}$ = 1.0; Table 2), but much larger than unity for CD_3OD reactants ($k_{ODH,CH3OH}/k_{ODH,CD3OD}$ = 2.4 ± 0.3, $k_{ODH}K_{1,CH3OH}/k_{ODH}K_{1,CD3OD}$ = 1.9 ± 0.5; Table 2), consistent with the kinetic relevance of H-abstraction at the C-atom. These measured KIE values were consistent with values calculated for both molecular and dissociative routes, but the enthalpic and entropic contributions to the calculated free energies of adsorption and activation overwhelmingly favor C−H activation from an undissociated CH_3OH molecule.[23]

The inhibition of ODH reactions by H_2O and the absence of any O_2 pressure effects with or without added H_2O (Figure 7) indicates that neither * nor OH/HO* are present at coverages detectable in the denominator of eq 2 and that inhibition by H_2O reflect the detectable coverage of H_2O−O* species at O* sites (instead of OH/HO* species; eqs 2, 3). DFT-derived molecular H_2O adsorption energies at redox sites are similar to those for CH_3OH adsorption ($\Delta E_{CH3OH-O*}$ = −7 kJ mol^{-1}, ΔE_{H2O-O*} = −9 kJ mol^{-1}; Table 1), leading to similar values of the measured equilibrium constants for H_2O (K_1') and CH_3OH (K_1) adsorption (K_1 = 3.6 kPa^{-1}, K_1' = 3.1 kPa^{-1}; Table 3), thus supporting the conclusion that they adsorb competitively on O* during CH_3OH ODH catalysis.

The lack of O_2 pressure effects on ODH rates (Figure 7, eq 3) suggest that reduced centers are present as minority species, apparently because of rapid O_2 activation steps. These reduced centers are therefore kinetically silent, but can be detected in UV−vis spectra measured during ODH reactions, because reduction causes the appearance of d−d electronic transitions in the pre-edge regions of the POM electronic spectra. The

Table 1. DFT-Derived (PW91-PAW) Structures and Formation Energies (in kJ mol^{-1}) of Adsorbed H_2O and CH_3OH Species at Acid and Redox Sites on $H_3PMo_{12}O_{40}$ Cluster

Adsorbate	Redox site	Acid site	
	Molecular adsorbate	Monomers	Protonated dimers
H_2O	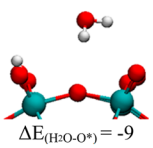 $\Delta E_{(H2O-O*)}$ = -9	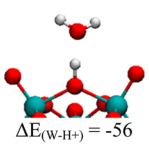 $\Delta E_{(W-H+)}$ = -56	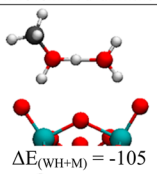 $\Delta E_{(WH+M)}$ = -105
CH_3OH	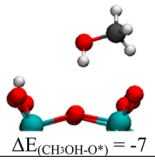 $\Delta E_{(CH3OH-O*)}$ = -7	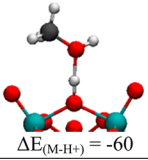 $\Delta E_{(M-H+)}$ = -60	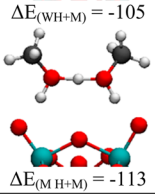 $\Delta E_{(M H+M)}$ = -113

DOI: 10.1021/cs501599y
ACS Catal. 2015, 5, 666−682

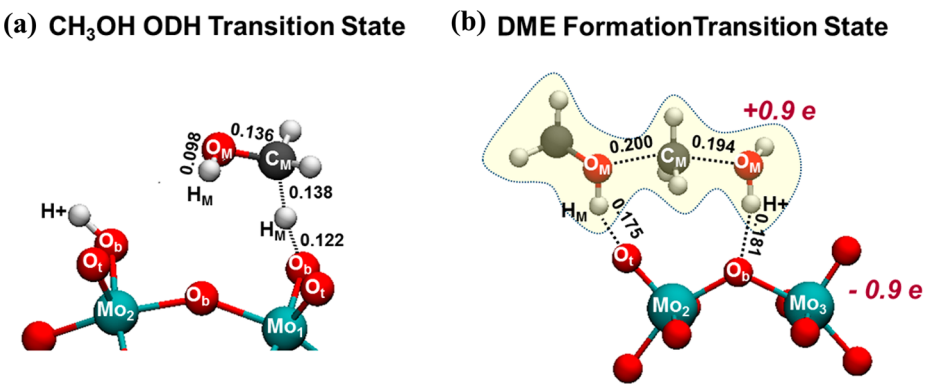

Figure 9. Kinetically relevant transition states prevalent for (a) CH_3OH ODH[23] and (b) DME formation[24] reactions on $H_3PMo_{12}O_{40}$ clusters. Atomic labels reflect C-, O- and H-atoms of methanol molecules (C_M, O_M, H_M, respectively) and Mo, bridging O and terminal O-atoms of POM clusters ($Mo_{1/2/3}$, O_b, O_t, respectively). Bond distances are reported in nm.

Table 2. Kinetic Isotope Effects for Rate Constants for ODH and DME Formation Reactions in $CH(D)_3OH(D)$-O_2 Mixtures on H_3PMo/SiO_2 (0.16)

	measured KIE values		calculated KIE values[c]	
rate constant[a]	CH_3OH/CD_3OD	CH_3OH/CH_3OD[b]	CH_3OH/CD_3OD	CH_3OH/CH_3OD
$k_{ODH}K_1$	1.9 (±0.5)	1.0	2.4	0.9
k_{ODH}	2.4 (±0.3)	1.0	2.9	1.0
k_{mono}	1.1 (±0.1)	1.0	0.9	-
k_{dimer}	0.7 (±0.2)	1.0	0.3	-

[a]Obtained by regressing rate data to the integral form of eqs 3 and 9 (433 K, 20 kPa O_2). [b]Rates were measured only at 4 kPa CH_3OD pressure (were nearly identical to CH_3OH rates), hence uncertainties could not be estimated. [c]Values calculated using DFT (PW91-PAW) and statistical mechanical treatments described in ref 23.

Table 3. Rate and Equilibrium Constants for CH_3OH ODH and DME Formation, Number of Protons Per Cluster Titrated by DTBP (n_{H+}), Edge Energy of the LMCT Band in UV−vis Spectra (E_{LMCT}), Reaction-Averaged HAE (<HAE>) and Deprotonation Energy (DPE) Values Obtained from DFT, for $H_3PMo_{12}O_{40}$, $H_4SiMo_{12}O_{40}$ and $H_3PW_{12}O_{40}$ Clusters[a]

quantity	$H_3PMo_{12}O_{40}$[b]	$H_4SiMo_{12}O_{40}$[b]	$H_3PW_{12}O_{40}$[c]
ODH rate and equilibrium constants			
$k_{1,ODH}$ (= $k_{ODH}K_1$) (kPa POM ks)$^{-1}$	6.5 (±1.2)	6.2 (±2.7)	--
K_1 (kPa)$^{-1}$	3.5 (±0.8)	5.4 (±2.7)	--
K_1' (kPa)$^{-1}$	3.1 (±0.7)	3.9 (±1.9)	--
DME formation rate and equilibrium constants			
k_{mono} (kPa H^+ ks)$^{-1}$	5.2 (±0.4)	4.8 (±0.8)	624
k_{dimer} (= k_{mono}/K_D) (H^+ ks)$^{-1}$	9.5 (±0.8)	8.9 (±1.6)	45
n_{H+}	2.5	2.2	2.0
$E_{H\text{-}L}$ (eV)[d]	1.92	1.97	2.55
E_{LMCT} (eV)	2.45	2.54	3.25
<HAE> (kJ mol^{-1})[e]	−302	−301	−224
DPE (kJ mol^{-1})[f]	1103	1125	1081

[a]Reported uncertainties reflect 95% trust intervals. [b]Rate constants obtained by regression of rates to integral forms of eqs 3 and 9 (433 K, 20 kPa O_2). [c]Rate constants and n_{H+} values at 433 K from ref 10. [d]Obtained from periodic DFT calculations in VASP (PW91-PAW). [e]Calculated using eq 13. [f]Calculated using methods described in ref 24 (PW91-USPP).

detection of such reduced centers is essential to confirm the proposed mechanism and to probe the nature and dynamics of the fast reoxidation steps. Next, we probe these reduced centers using UV−vis spectra during CH_3OH-O_2 reactions and compare the observed spectral features with those predicted from theoretical treatments and the effects of reactant and product concentrations on their intensity with those expected from the elementary steps in Scheme 2.

3.4. Detection of Reduced Centers by UV−vis Spectra during CH_3OH-O_2 Catalysis. Figure 10a shows the UV−vis spectra for H_3PMo/SiO_2(0.16) at 433 K before and during CH_3OH-O_2 reactions (1 kPa CH_3OH, 20 kPa O_2). The broad absorption band evident before reaction arises from O → Mo ligand-to-metal charge transitions (LMCT) with a band edge-energy of 2.45 eV (determined using methods described in Section 2.4). This edge energy reflects excitation of an electron from the highest occupied molecular orbital (HOMO), consisting of p-orbitals residing at O-atoms, to the lowest unoccupied molecular orbital (LUMO), consisting of d-orbitals at Mo-atoms.[41] This LMCT band weakened only very slightly during CH_3OH-O_2 reactions, but additional features emerged in the pre-edge region (0.7−2.5 eV) upon contact with CH_3OH-O_2 reactants. These pre-edge features arise from d−d electronic transitions made possible by electrons introduced into previously

DOI: 10.1021/cs501599y
ACS Catal. 2015, 5, 666−682

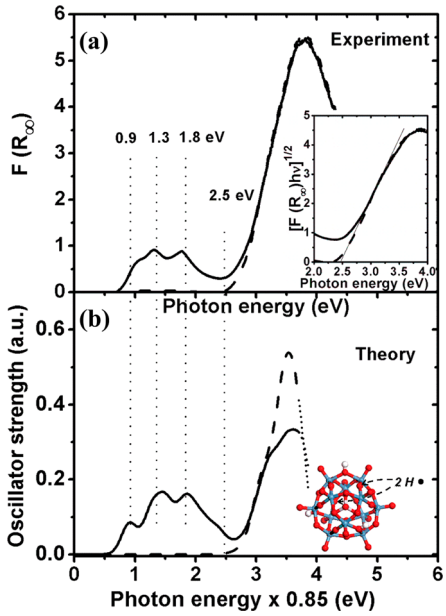

Figure 10. (a) Experimental diffuse reflectance UV−vis spectra of H_3PMo/SiO_2 (0.16) in O_2 (dashed curve, 20 kPa O_2) and during CH_3OH-O_2 reactions (solid curve, 4 kPa CH_3OH, 20 kPa O_2) at 433 K. The inset shows the UV−vis spectra plotted as $[F(R_\infty)\ h\nu]^{1/2}$, a form required to obtain accurate absorption edge energies. (b) Time-dependent DFT-derived (Gaussian, B3LYP) UV−vis spectra on oxidized H_3PMo cluster (dashed curve) and cluster reduced by sequentially adding two H-atoms to most stable locations (solid curve; inset shows the locations). Dotted parts of the calculated spectra reflect excited states at energies >3.75 eV that were not fully captured within 300 excited states obtained from TD-DFT calculations.

empty d-orbitals at Mo^{6+} centers upon reduction;[42] their intensities are proportional to the number of reduced centers and thus to the extent of reduction of the catalyst during ODH catalysis.[42]

Figure 10b shows UV−vis spectra calculated using TD-DFT methods for a fully oxidized intact $H_3PMo_{12}O_{40}$ cluster and for this cluster after a two-electron reduction caused by adding two H-atoms ($H_5PMo_{12}O_{40}$) at their lowest energy locations (to mimic the placement of the two H-atoms formed via the sequential H-abstraction steps required in the ODH reaction; Scheme 2, Step 2). The abscissa energies in these theoretical spectra were corrected by a scaling factor (0.85) to account for the well-known DFT inaccuracies in describing the energies of the excited states formed in photon-induced transitions;[43] the scaling factor was chosen so as to bring the edge energy to the value measured on these POM clusters (~2.5 eV, Figure 10a) from a TD-DFT-derived estimate of ~3.0 eV in the uncorrected spectra. The calculated spectrum of the reduced cluster shows pre-edge features (near 0.7−2.5 eV, Figure 10b) similar to those in the UV−vis spectra for H_3PMo/SiO_2 measured during catalysis (Figure 10a). The ratios of the pre-edge to the LMCT band intensities were weaker in the measured spectra than in the spectra calculated for a two-electron reduction of each POM cluster, indicating that the ODH-induced spectral changes reflect a small extent of reduction in POM clusters during ODH redox cycles.

The pre-edge features in the UV−vis spectra were calculated on $H_3PMo_{12}O_{40}$ clusters for the addition of the two H-atoms at different O-atoms (i.e., different OH/HO* locations; Scheme 2) and for a cluster with an O-vacancy at one location (* site; Scheme 2). All spectra (shown in the SI) exhibit pre-edge features of similar energy and intensity at 1.8 eV (Figure 10), but different lower energy features (0.7−1.6 eV), which vary in intensity and shape for different * and OH/HO* locations. Therefore, we conclude that the intensity at 1.8 eV accurately reflects the relative concentrations of reduced centers during ODH catalysis at different CH_3OH, O_2, and H_2O pressures during catalysis.

Next, we compare these effects of reactant and product concentrations on pre-edge intensities (at 1.8 eV) with those predicted by the elementary steps in Scheme 2. The concentration of reduced centers (n_r = * + OH/HO*) derived from the elementary steps in Scheme 2 is given by

$$\frac{n_r}{[\mathrm{POM}]} = \frac{1 + K_4P_{H_2O}}{1 + K_4P_{H_2O} + \frac{2k_5P_{O_2}}{k_{ODH}K_1P_{CH_3OH}}(1 + K_1P_{CH_3OH} + K_1'P_{H_2O})} \quad (6)$$

(derivation in SI), where the constants are defined as in eq 2 and Scheme 2. The denominator terms reflect the relative concentrations of (*), (OH/HO*), (O*), (CH_3OH-O*) and (H_2O−O*) in the order of their appearance. When reduced centers are minority species (Figure 7, eq 2), eq 6 becomes

$$\frac{n_r}{[\mathrm{POM}]} = \left(\frac{1 + K_4P_{H_2O}}{2k_5P_{O_2}}\right)\left(\frac{k_{ODH}K_1P_{CH_3OH}}{1 + K_1P_{CH_3OH} + K_1'P_{H_2O}}\right) \quad (7)$$

The ratio of pre-edge to LMCT band intensity (~ n_r) as a function of CH_3OH, H_2O and O_2 pressure (Figure 11) agrees

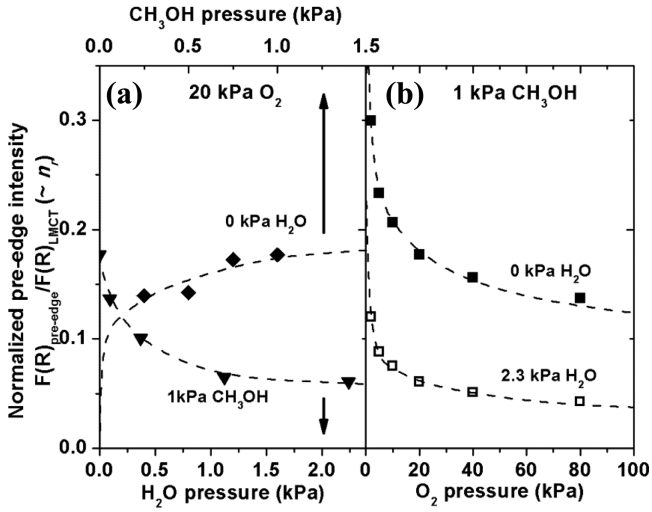

Figure 11. Intensity of the pre-edge region of UV−vis spectra (at 1.8 eV; Figure 10) normalized by the intensity of LMCT band ($I_{pre\text{-}edge}/I_{LMCT}$ ~ n_r), during CH_3OH-O_2 reactions, as functions of (a) CH_3OH and H_2O pressures, and (b) O_2 pressures. Dashed curves represent qualitative trends.

well with the trends derived from eq 7. The n_r values increased nonlinearly with CH_3OH pressure (Figure 11a), consistent with an initial increase in the rate of the reduction elementary steps at low CH_3OH pressures, which ultimately reaches a constant value as POM clusters reach saturation CH_3OH-O* coverages at higher pressures (Figure 6a). Increasing O_2 and H_2O pressures decreased n_r values (Figure 11b), consistent with faster reoxidation at higher O_2 pressures and with the lower reduction rates caused by higher H_2O−O* coverages at higher H_2O pressures. These data also show that H_2O does not adsorb at

DOI: 10.1021/cs501599y
ACS Catal. 2015, 5, 666−682

detectable coverages on vacancies (to form OH/HO*), because such process would cause H_2O to increase the number of reduced centers (eq 7). We conclude from these trends and their theoretical underpinnings that pre-edge features correspond to reduced centers present as minority species and acting as intermediate species in ODH turnovers. The mechanistic interpretation of ODH rates shown as Scheme 2 accounts for both measured ODH rates and for the observed concomitant changes in the concentration of reduced centers detected in the UV−vis spectra during catalysis.

These changes in the extent of reduction with reactant and product concentrations (Figure 11) are consistent with the functional form of eq 7 but are not quantitatively described by this equation. This appears to reflect a catalytically irrelevant reduction that occurs gradually during exposure to reactants, which is evident from nonzero asymptotic pre-edge intensities at high O_2 pressures (Figure 11b) that are not consistent with the monotonic decrease to zero values indicated by the form of eq 7. Such slow reduction processes may reflect a change in the reduction properties as clusters slightly change their extent of hydroxylation during catalysis, evident from their substoichiometric and hydration-dependent titrant uptakes (Section 3.1; Figure 3). They could also arise from a structural modification that occurs slowly while POM clusters temporarily exist in their reduced state during a catalytic turnover and which may decrease their reoxidation rates; these slower reoxidation events would lead to greater extent of reduction during ODH catalysis but would not affect turnover rates (as observed experimentally) as long as oxidized centers (O*, CH_3OH-O*, H_2O−O*; Scheme 2) remain the MASI and reduced centers minority species; their concentrations do not influence rate, but their concentrations are detectable by their UV−vis spectra and depend on their reoxidation rates.

The dynamics of the elementary steps that reoxidize the reduced POM clusters are inaccessible to steady-state kinetic measurements (Section 3.3, Scheme 2), because O_2 activation at reduced centers (*, Scheme 2) is much more rapid than the steps that reduce the oxidized centers (O*, Scheme 2) at all reaction conditions. The time scales characteristic of changes in the number of reduced centers in response to a change in the reductant to oxidant ratio (CH_3OH/O_2) and their mechanism based interpretations can provide estimates of reoxidation rate constants intrinsically normalized by the number of active sites, as shown previously on alumina supported VO_x domains.[42] Such methods are being developed to probe the effects of reductant and oxidant pressures on reoxidation rate constants on POM clusters, along with DFT calculations to compare the energies of intermediates and transition states involved in proposed reoxidation pathways, and to infer descriptors of reoxidation dynamics from such measurements and calculations.

3.5. Elementary Steps and Effects of Reactant Pressures for DME Formation Rates. Here we examine the rates of parallel DME formation pathways and their mechanistic interpretations. Scheme 3 shows the elementary steps for CH_3OH dehydration reactions (on Brønsted acid sites), which proceed concurrently with ODH steps (on O* sites). The steps in Scheme 3 were previously shown to mediate such reactions on W-based POM clusters ($H_{8-n}X^{n+}W_{12}O_{40}$, X^{n+} = P^{5+}, Si^{4+}, Al^{3+}, and Co^{2+}) based on kinetic data combined with theoretical treatments.[10]

H-bonded CH_3OH (M−H^+) species form via interactions with protons in quasi-equilibrated steps (Step 1, in Scheme 3) and then react with another CH_3OH in quasi-equilibrated steps

Scheme 3. Proposed Elementary Steps for CH_3OH Dehydration to Dimethyl Ether (DME) on Brønsted Acid Sites of POM Clusters

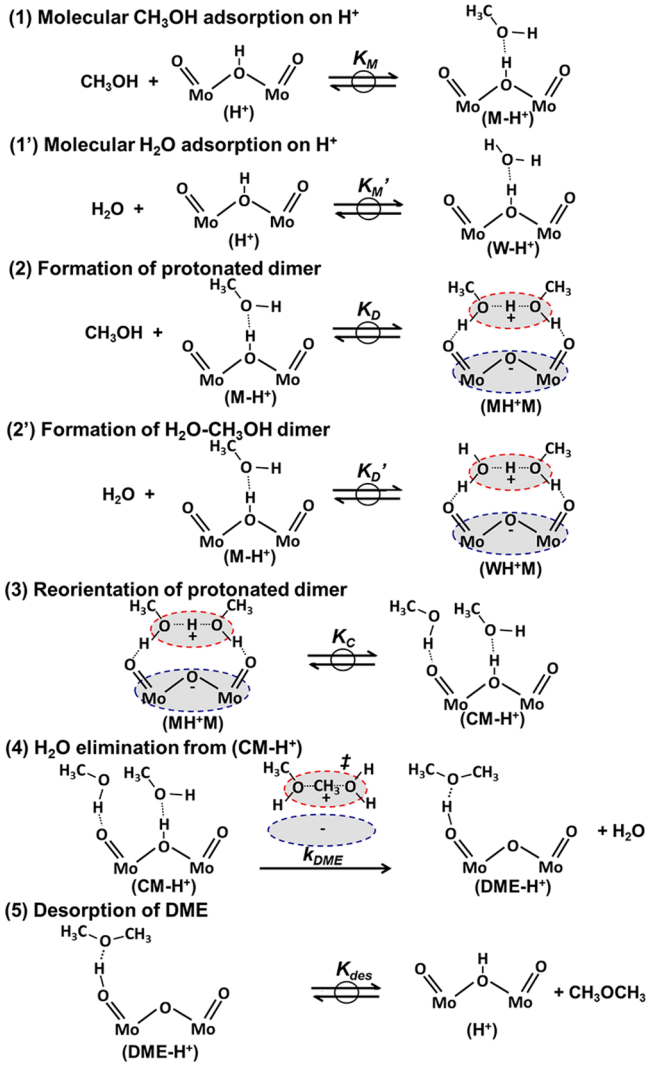

involving proton transfer from POM clusters to H-bonded CH_3OH species to form protonated dimers (MH^+M, Scheme 3). The dimers exist as ion-pairs stabilized by electrostatic interactions with the POM conjugate anions (Step 2, Scheme 3); they rearrange into less stable, but properly oriented, "co-adsorbed monomer species" (CM−H^+, Step 3 in Scheme 3) to form DME and eliminate H_2O in a concerted manner (Step 4 in Scheme 3). Step 4 is mediated by late ion-pair transition states reminiscent of those involved in S_N2-type reactions, in which the O-atom in CH_3OH carries out a nucleophilic attack on the electrophilic methyl cation with H_2O as the stable leaving group, aligned in the quasi-linear structure required for proper orbital overlap (Step 4 in Scheme 3). A turnover is completed by desorption of DME to reform protons (Step 5 in Scheme 3). H_2O can interact with protons or with H-bonded CH_3OH to form H-bonded water species (W−H^+; Step 1′, Scheme 3) or water−methanol dimers (WH^+M; Step 2′, Scheme 3).

Quasi-equilibrated CH_3OH adsorption and irreversible H_2O elimination steps lead to the DME formation rate equation (derived in SI):

DOI: 10.1021/cs501599y
ACS Catal. 2015, 5, 666−682

$$\frac{r_{DME}}{[H^+]} = \frac{k_{DME} K_M K_C K_D P_{CH_3OH}^2}{1 + K_M P_{CH_3OH} + K_M' P_{H_2O} + K_M K_D P_{CH_3OH}^2 + K_M K_D' P_{CH_3OH} P_{H_2O}} \quad (8)$$

(H⁺) (M-H⁺) (W-H⁺) (MH⁺M) (WH⁺M)

in which $[H^+]$ is the number of protons (obtained from DTBP titration during catalysis; Section 3.1). K_M, K_M', K_C, K_D, and K_D' are the equilibrium constants for the formation of CH_3OH monomers, H_2O monomers, coadsorbed CH_3OH species, protonated CH_3OH dimers and CH_3OH-H_2O dimers, and k_{DME} is the rate constant for DME formation from coadsorbed species. The terms in the denominator of eq 8 represent the ratio of the concentrations of the listed species to the concentration of free protons (H^+).

DME formation rates show a Langmuir-type nonlinear dependence on CH_3OH pressure (Figure 6b); such kinetic dependences and theoretical studies on W-based POM clusters[10] indicate that monomer (M−H⁺) and dimer (MH⁺M) species prevail at POM surfaces at all relevant methanol pressures and that the term for unoccupied H^+ in the denominator of eq 8 is negligible. DME formation rates were unaffected by H_2O pressure (Figure 7, 8), indicating that H_2O-containing terms are not present in the denominator term of eq 8. In this case, eq 8 becomes

$$\frac{r_{DME}}{[H^+]} = \frac{k_{DME} K_C K_D P_{CH_3OH}}{1 + K_D P_{CH_3OH}} \quad (9)$$

The regression of the rate data shown in Figure 6b to the functional form of eq 9 gives a first-order rate constant (k_{mono}) that reflects the energy of the late-ion pair DME formation TS ($\Delta E^{\ddagger}_{TS,DME}$) with respect to a H-bonded CH_3OH monomer (ΔE_{M-H^+}) and a gaseous CH_3OH molecule ($\Delta E_{CH3OH(g)}$):

$$k_{mono} = k_{DME} K_C K_D \sim \exp(-(\Delta E^{\ddagger}_{TS,DME} - \Delta E_{M-H^+} - \Delta E_{CH_3OH(g)})/RT) \quad (10)$$

and a zero-order rate constant (k_{dimer}) that reflects the energy of the same TS but with respect to a protonated dimer intermediate (ΔE_{MH^+M}):

$$k_{dimer} = k_{DME} K_C \sim \exp(-(\Delta E^{\ddagger}_{TS,DME} - \Delta E_{MH^+M})/RT) \quad (11)$$

The structures of reactive intermediates (monomer and protonated dimer) and of late ion-pair DME formation TS previously derived from DFT calculations on W and POM clusters[10,24] are shown in Table 1 and Figure 9, respectively.

The measured and DFT-derived KIE values for the first-order DME formation rate constants are near unity for CD_3OD and CH_3OD reactants (measured: $k_{mono,CH3OH}/k_{mono,CH3OD}$ = 1.0, $k_{mono,CH3OH}/k_{mono,CD3OD}$ = 1.1 ± 0.1; calculated: $k_{mono,CH3OH}/k_{mono,CD3OD}$ = 0.9; Table 2), suggesting that the kinetically relevant transition state does not involve the activation of either C−H(D) or O−H(D) bonds. These values are consistent with the calculated TS structures (Figure 9b), which involves the transfer of the CH_3^+ group from one CH_3OH molecule to another one without any detectable C−H elongation along the reaction coordinate. The proton resides near the O-atom in $H_3PMo_{12}O_{40}$ (O_{POM}−H distance, 0.105 nm) in the monomer intermediates and away from the O-atom in CH_3OH (0.145 nm);[24] at the transition state, the O_{POM}−H bond cleaves (0.181 nm distance) and a new O_{CH3OH}−H bond form (0.100 nm). The monomer and the TS have an equal number of fully formed C−H and O−H bonds, and neither C−H nor O−H stretching vibrational modes lie along the reaction coordinate. As a result, any isotopic effects for the transition state and the reference state cancel.

The measured KIE values for the zero-order DME formation rate constant are slightly smaller than unity (measured: $k_{dimer,CH3OH}/k_{dimer,CD3OD}$ = 0.7 ± 0.2 ; Table 2), while theoretical estimates are significantly smaller (calculated: $k_{dimer,CH3OH}/k_{dimer,CD3OD}$ = 0.3; Table 2); such KIE values reflect a thermodynamic isotope effect arising from the low vibrational frequency of the proton that lies between the two O_{CH3OH}-atoms in $(CH_3OH)_2H^+$ dimers (1703 cm^{-1} from DFT; structure in Table 1) compared with that of the O_{POM}−H structures in bare POM cluster (3728 cm^{-1}). This dimer resembles a "proton sponge cation,"[44] in which a proton is sandwiched between two O_{CH3OH}-atoms in a symmetric structure with nearly identical O−H bond lengths.[45] The potential energy surface for the H^+ oscillation in such structures reflects an overlap between individual O_{CH3OH}−H stretching potentials,[44] which cannot be described by a harmonic oscillator. As a result, the DFT-derived vibrational frequencies, which are calculated using such oscillators, tend to be inaccurate for such modes, thus leading to DFT-derived KIE estimates (0.3) that are smaller than measured values for k_{dimer} rate constants (0.7 ± 0.2).

DME formation rates were unaffected by H_2O pressures (Figure 6b, 7), suggesting that H_2O adsorbs more weakly than CH_3OH at proton sites, consistent with O-atom that act as a weaker base in H_2O than CH_3OH, as expected from H acting as a weaker electron donor than CH_3.[46] DFT-derived formation energies for H_2O monomer (W−H⁺, Scheme 3, eq 8) and H_2O−CH_3OH dimers (WH⁺M) are less exothermic than the corresponding CH_3OH monomer (M−H⁺) and dimer (MH⁺M) species (by 4 and 8 kJ mol^{-1}, respectively; Table 1), consistent with the lack of inhibition of DME rates by moderate H_2O pressures.

3.6. Ionic and Covalent Components of Deprotonation Energies as Reactivity Descriptors for Acid Catalysis. The first-order DME formation rate constant (k_{mono}) on Bronsted acid sites reflects the energy of an ion-pair transition state (Scheme 3; Figure 9b) relative to that for an uncharged CH_3OH monomer (M−H⁺, Scheme 3) and a gaseous CH_3OH molecule (eq 10).[10] The k_{mono} values measured previously on W-POM clusters with different central atoms decreased exponentially with their deprotonation energy (DPE),[10] defined as the energy required for removing a proton from its conjugate base to noninteracting distances (HA → H^+ + A^-); these DPE values represent a probe-independent measure of the strength of Brønsted acids.[7] The TS energies increased (k_{mono} decreased) with increasing DPE on clusters with different central atoms because the TS formation requires proton removal from the cluster; these effects of DPE are partly compensated by ion-pair interactions of TS cations with POM anions, leading to slopes smaller than unity in the TS energy versus DPE plots.[10] The k_{mono} values measured on Mo-POM clusters (H_3PMo/SiO_2 and H_4SiMo/SiO_2; Table 3) were much smaller than the values on W-POM clusters of equivalent DPE, suggesting that DPE is an essential but incomplete descriptor of reactivity.[24] The origin of such apparent disparity in the effect of DPE on the reactivity for the two classes of Brønsted acids (Mo and W POM) has been recently examined using theoretical methods that dissect DPE into ionic and covalent components; these components reflect electrostatic interaction between a proton and its conjugate anion (ionic), and the reorganization of anion charge induced by

DOI: 10.1021/cs501599y
ACS Catal. 2015, 5, 666−682

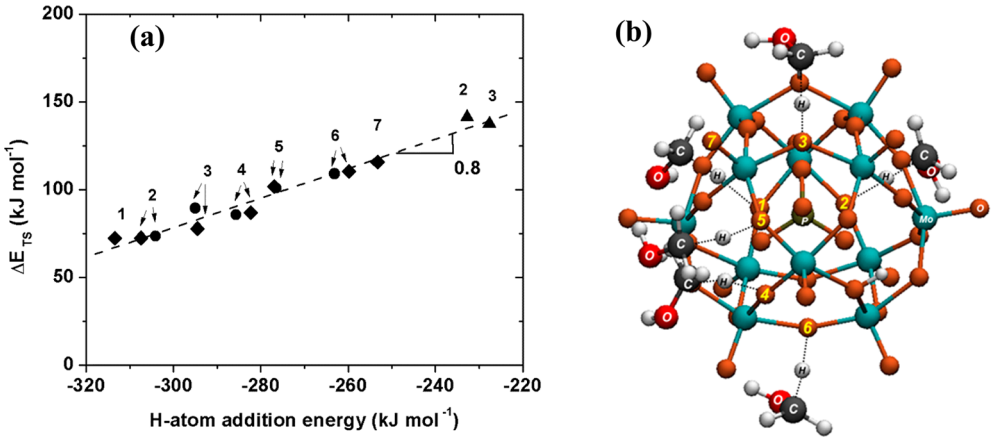

Figure 12. (a) DFT-derived energy of H-abstraction transition state relative to a gaseous CH_3OH molecule as a function of H-atom addition energy at different abstracting O-atoms (redox sites, O*) on $H_3PMo_{12}O_{40}$ (♦), $H_4SiMo_{12}O_{40}$ (●), $H_3PW_{12}O_{40}$ (▲) Keggin clusters. Dashed line reflects the best linear regression fit. (b) The locations of the abstracting O-atoms in (a) and the structures of transition states on $H_3PMo_{12}O_{40}$ cluster. Transition-state calculations were performed separately at each location.

the proton (covalent).[24] Mo-POM clusters have a larger covalent and a smaller ionic component of DPE than a W-POM cluster with the same DPE. Such covalency is disrupted upon deprotonation of the acid but not fully recovered by the ion-pair interactions between TS cation and the POM anion, leading to less stable TS on clusters with greater covalency (Mo-POM).[24] These results suggested that general reactivity descriptors for diverse classes of solid acids require separate assessments of ionic and covalent DPE components.[24] Changes in addenda atoms (W to Mo) did not affect the correlations of k_{dimer} with DPE significantly,[24] because k_{dimer} values reflect the energy of a charged transition state with respect to a charged dimer intermediate (eq 11), resulting in the cancellation of the effects deprotonation.

3.7. Reactivity Descriptors and Compositional Effects for Oxidation Catalysis. Measured CH_3OH ODH rates and their kinetic interpretations are combined here with theoretical estimates of reaction and activation energies and of catalyst properties to probe the consequences of composition and the most appropriate descriptors of reactivity in redox and acid catalysis.

The first-order ODH rate constant ($k_{1,ODH}$) reflects the energy of the transition state for C−H activation in molecularly adsorbed CH_3OH (Step 2, Scheme 2) relative to a gaseous CH_3OH molecule (eq 4). The formation of this TS involves the transfer of an electron into the LUMO of the POM cluster, which consists of d-orbitals at Mo^{6+} centers,[41] and the coupled transfer of a H^+ to an O-atom. The difference between charges on atoms in the TS and on the respective atoms in the initial state (CH_3OH-O*, Scheme 2) were calculated from DFT-derived charge distributions based on the Bader method[47,48] (values shown in the SI). These charge differences indicate that the TS has a 0.57 e charge density located in the previously unoccupied d-orbitals at Mo centers of the cluster while the remaining density (~0.4 e) resides near the H-atom (H^+) being transferred in Step 2 (Scheme 2). The C−H bond in the TS (0.138 nm, Figure 9a) is much longer than that in its CH_3OH-O* precursor (0.110 nm), while the O_{POM}−H bond (0.122 nm) resembles that in the product of Step 2 (0.100 nm). These charges and bond-distances are consistent with an H-abstraction TS that lies late along the reaction coordinate for the transfer of both the electron and the proton required to form the products of the C−H activation step. As a result, the TS energies depend strongly on the energies of the product state and specifically that of the O−H bond that forms between the abstracted H-atom and the O-atom in the POM cluster.

The O → Mo LMCT bands in the UV−vis spectra (Figure 10) reflect the excitation of an electron from the HOMO to the LUMO;[41] the energies of these transitions may serve as an indirect proxy of the energy of the LUMO that accepts the electron in H-abstraction steps, since theoretical treatments indicate that HOMO energies are relatively insensitive to composition for Keggin POM clusters with Mo, W and V addenda atoms.[41] Therefore, the energy of the LMCT band-edge in the UV−vis spectra (inset in Figure 10a) represents a plausible experimental descriptor of the stability of the H-abstraction transition states for different POM compositions.

Measured $k_{1,ODH}$ values are insensitive to changes in the central atom of Mo-based POM clusters (6.5 and 6.2 $(kPa.POM.ks)^{-1}$ on H_3PMo/SiO_2 and H_4SiMo/SiO_2, respectively; Table 3) but decrease significantly when the addenda atoms are changed from Mo to W (ODH rates undetectable on H_3PW/SiO_2; < 0.01 $(kPa.POM.ks)^{-1}$; Table 3). These trends are consistent with values of HOMO−LUMO gaps (E_{H-L}) and LMCT edge energies (E_{LMCT}) that are similar for H_3PMo and H_4SiMo clusters, but much higher for H_3PW clusters (Table 3). The higher E_{H-L} and E_{LMCT} values for W-POM reflect a higher LUMO energy, which depends on the identity of addenda atoms but not of central atoms, because the LUMO consists of the d-orbitals in these addenda atoms. E_{LMCT} values thus represent appropriate descriptors of reactivity for the clusters shown in Table 3. The $k_{1,ODH}$ values on a wider variety of oxide compositions (e.g., V-substituted POM, supported oxide domains), however, do not necessarily behave as a single-valued function of E_{LMCT}, because such values are affected by the relaxation of the electron excited to LUMO due to its interaction with the "hole" created by the excitation of the HOMO electron.[49] Electron−hole interactions are stronger for more localized LUMO orbitals and vary with the composition of semiconductor materials.[50] Such variations do not reflect compositional effects relevant to the energy of the C−H activation transition states, because the latter require the injection of an additional electron into the LUMO from the reacting CH_3OH molecules, without the concomitant formation of a hole in the HOMO. As a result, E_{LMCT} values may not change monotonically with LUMO energies or with ODH rate constants

DOI: 10.1021/cs501599y
ACS Catal. 2015, 5, 666−682

on classes of oxide materials that differ significantly in the extent of relaxation of excited electrons.

A more rigorous descriptor, accessible through theoretical estimates, but only for catalysts with known structure, is the energy involved in adding a H-atom (or H-atom addition energy; HAE) to each O-atom in a given POM cluster (e.g., an $H_3PMo_{12}O_{40}$ cluster):

$$\mathrm{HAE} = E(\mathrm{H_4PMo_{12}O_{40}}) - E(\mathrm{H_3PMo_{12}O_{40}}) - E(\mathrm{H}) \quad (12)$$

where $E(H_3PMo_{12}O_{40})$ and E $(H_4PMo_{12}O_{40})$ reflect the DFT-derived energies for the POM cluster before and after H-atom addition, whereas $E(H)$ reflects the energy of an isolated H-atom at a noninteracting distance from the POM cluster. Such descriptors probe the energy of the O−H bond that forms at the late H-abstraction transition state in the C−H activation step (Step 2, Scheme 2). These HAE values reflect the combined energy to introduce an electron into the LUMO of the cluster and to add a proton to an O-atom; therefore, HAE values describe transition-state energies more accurately than the LMCT electronic excitation energies in UV−vis spectra.

Figure 12 shows DFT-derived energies for the H-abstraction transition state (referenced to a gaseous CH_3OH molecule, as relevant to $k_{1,ODH}$ values) at each distinct O-atom in $H_3PMo_{12}O_{40}$, $H_4SiMo_{12}O_{40}$ and $H_3PW_{12}O_{40}$ clusters as a function of the HAE of each O-atom. The calculated TS energies that reflect enthalpies at 0 K (uncorrected by zero-point vibrational energies) are shown because the effects of vibrational frequencies and entropy contributions are expected to be similar at all locations and for all compositions. TS energies and HAE values depend strongly on the location of O-atoms within POM clusters and on the composition of the clusters in a manner that gives TS energies proportional to HAE values. Calculated TS energies at one O-atom location on V-substituted POM clusters,[23] as a function of HAE of that O-atom, also followed the same trend as shown in Figure 12, suggesting that CH_3OH reactivity is a single-valued linear function of HAE. This function has a slope near unity (Figure 12, slope = 0.8), consistent with the late nature of the H-abstraction TS and with the relevance of HAE values as an accurate descriptor of ODH reactivity.

The HAE values at each O-atom location are depicted visually as two-dimensional projections of $H_3PMo_{12}O_{40}$, $H_4SiMo_{12}O_{40}$ and $H_3PW_{12}O_{40}$ clusters in Figure 13. The bridging and terminal O-atoms are represented by interconnecting lines and as circles at the intersections of lines, respectively. Protons at O-atoms are shown as small white circles, while white triangles denote the location of O-atoms tetrahedrally arranged around the POM central atom. Bridging and terminal O-atoms are labeled with colors that reflect HAE values between −325 kJ mol^{-1} (red) and −200 kJ mol^{-1} (blue) (shown in the color-scale in Figure 13). A more negative HAE value reflects a more stable O−H bond and, by inference (Figure 12), a more stable H-abstraction TS and a more reactive O* species. HAE values on all POM compositions are more negative at bridging than terminal O-atoms (Figure 13), indicating that bridging O-atoms predominantly account for the ODH reactivity of these clusters (e.g., the most negative HAE values for terminal and bridging O-atoms in $H_3PMo_{12}O_{40}$ are −261 and −313 kJ mol^{-1}, respectively; Figure 13). The presence of a proton at a bridging O-atom leads to a much less negative HAE values (lowest HAE at Brønsted OH in $H_3PMo_{12}O_{40}$ is −265 kJ mol^{-1}) than at bare O* sites (−313 kJ mol^{-1}); therefore, the most reactive O* sites on a POM cluster are bridging atoms that reside away from the charge-balancing protons. These HAE

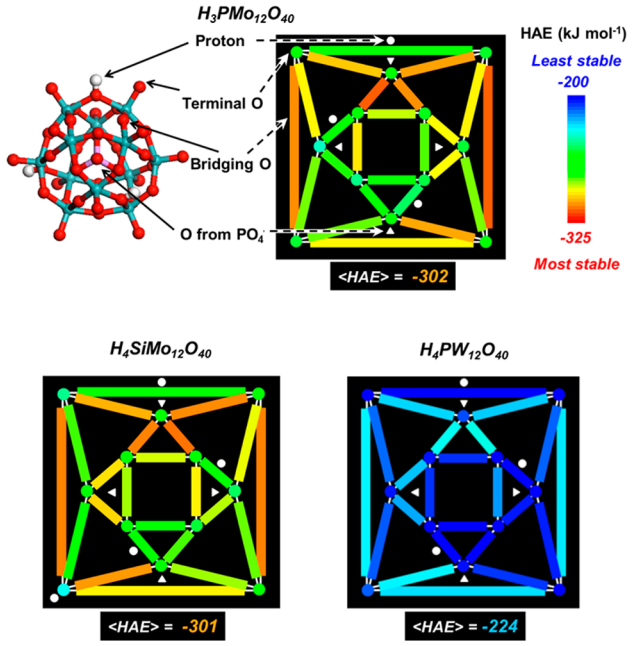

Figure 13. Distribution of H-addition energies (HAE) at all surface O-atoms on $H_3PMo_{12}O_{40}$, $H_4SiMo_{12}O_{40}$ and $H_3PW_{12}O_{40}$ clusters represented using color maps on two-dimensional projections of the clusters. <HAE> values reflect a reaction average over HAE values calculated at each distinct O-atom in a cluster, obtained using eq 13

values indicate that acid and redox reaction proceed independently at protons (acid) and at bare (redox) O-atoms. Such conclusions about independent pathways and locations of acid and redox reactions are consistent with experimental inferences of site their requirements (Section 3.2), because H_2O, which competes with CH_3OH on redox sites, does not affect DME formation rates, while DTBP molecules, which titrate acid sites, do not fully suppress ODH rates.

Calculated HAE values and H-abstraction TS energies vary significantly with O-atom location in a POM cluster (Figures 12, 13), while the measured ODH turnover rates reflect a reactivity that averages over the TS structures at all O* sites. The rate at each O* site depends exponentially on the free energy of activation at that site, which, in turn, depends linearly on the HAE value at that site (Figure 12). As a result, the free energies corresponding to measured ODH rate constants reflect an exponentially weighted average of transition-state free energies at all O-atoms of the POM cluster that can be rigorously described by a reactivity-averaged HAE value (<HAE>) given by (derivation in the SI, Section S10):

$$\exp\left(\frac{-m < \mathrm{HAE}>}{RT}\right) = \frac{1}{n_{O^*}} \sum_{i=1}^{n} \exp\left(\frac{-m\mathrm{HAE}_i}{RT}\right) \quad (13)$$

where m, O*, and n_{O^*} reflect the slope of the transition-state energies versus HAE plot (m = 0.8 in Figure 12), surface O-atoms of POM clusters, and the total number of such O-atoms, respectively. This averaging of the local changes in redox properties accounts for more rigorous reactivity descriptors than the global minimum energy differences reflected in HOMO−LUMO gaps and indirectly probed by LMCT excitation energies.

The reaction averaged HAE values are similar on $H_3PMo_{12}O_{40}$ and $H_4SiMo_{12}O_{40}$ clusters (<HAE> = −302, −301 kJ mol^{-1}, respectively; Figure 13) but much less negative on $H_3PW_{12}O_{40}$ clusters (−224 kJ mol^{-1}; Figure 13); these results are consistent

DOI: 10.1021/cs501599y
ACS Catal. 2015, 5, 666−682

with the similar ODH rates and LUMO and LMCT energies for $H_3PMo_{12}O_{40}$ and $H_4SiMo_{12}O_{40}$ and the lower ODH turnover rates and higher LUMO energies and LMCT excitation energies for $H_3PW_{12}O_{40}$ clusters (Table 3). The HAE values exhibit a single-valued correspondence with the stability of the kinetically relevant H-abstraction TS at each O-atom (Figure 12) and, when averaged over all O-atoms of a given POM composition, represent a rigorous and complete reactivity descriptor derived from theory (eq 13, derivation in SI, Section S10). Our ongoing studies seek to extend these concepts to describe the effects of the number and location of V-atoms substituted into Mo and W based Keggin POM clusters on ODH turnover rates, <HAE> values and LMCT energies. Such composition-function relations can only be derived from compositionally diverse materials with known and uniform structures that allow unambiguous comparisons between experiments and theory. These relations developed on well-defined materials can be used together with oxidation reactivity measurements on materials with nonuniform or uncertain structures to estimate their apparent <HAE> values and to infer plausible structures of their active sites.

4. CONCLUSIONS

Reactions of CH_3OH-O_2 mixtures are used to probe acid and redox reactivity by combining kinetic, isotopic, and spectroscopic methods on well-defined Mo-based polyoxometalate (POM) clusters together with theoretical calculations of kinetically relevant intermediates and transition states and accessible catalyst descriptors. Solid-state ^{31}P-MAS NMR, TEM, and titrations of protons with DTBP showed that Mo-POM clusters supported on SiO_2 at low coverages remain as intact Keggin structures that undergo partial dehydroxylation of Brønsted acid protons during reactions under anhydrous conditions but remain nearly intact when reactions are carried out with H_2O added to CH_3OH-O_2 reactants. The effects of CH_3OH and O_2 pressures on the ODH rates and their mechanistic interpretations, H-D kinetic isotope effects (for CH_3OD and CD_3OD reactants), and electronic transitions of reduced centers evident in the UV−vis spectra during catalysis are consistent with redox sites that catalyze CH_3OH ODH via Mars−van Krevelen redox cycles. Reduction and oxidation elementary steps, which activate C−H bond in molecularly adsorbed CH_3OH at lattice O-atoms and O_2 at reduced centers, respectively, are kinetically coupled within these catalytic sequences. The dependence of rates on reactant pressures show that reduction steps limit ODH rates while the reoxidation steps are kinetically irrelevant, which leads to small extents of reduction during catalysis.

The first-order ODH rate constant ($k_{1,ODH}$) decreased significantly when the Mo addenda atoms of POM clusters were replaced by W, because electrons in the kinetically relevant reduction step occupy the lowest unoccupied molecular orbitals (LUMO) of clusters that consist of the d-orbitals of addenda atoms. The TS energies depend strongly on the energy to add H-atom to O* sites in POM clusters because the TS appears late along the reaction coordinate leading from the C−H bond in methanol to the product O_{POM}-H bond after C−H activation. Energies of H-abstraction TS and the H-addition energy (HAE) are functions of location on the POM clusters; consequently, reaction averaged HAE values that include contributions from all cluster O-atoms are required to rigorously describe the ODH reduction rate constants on different cluster compositions. ODH rate constants were weakly influenced by the identity of the central atoms (P or Si) for Mo-clusters; this weak dependence was also reflected in similar HAE values. Such composition function relations are being developed over a broader compositional range by including V-substituted POM clusters, which can then be used to obtain estimates of HAE values on materials with uncertain structure based on their measured reactivity, and to infer from such estimates the plausible reactive structures of such materials.

DME formation rate dependences are consistent with the set of elementary steps developed previously for monofunctional W-POM clusters. CH_3OH molecules adsorb sequentially as H-bonded monomers or protonated dimers and form DME and eliminate H_2O in a concerted step mediated by carbenium-ion TS. Mo-based POM clusters are much less reactive for DME formation than W-based Keggin clusters, even at similar deprotonation energies (DPE) for the two classes of acids. These reactivity differences reflect different ionic and covalent components of ion-pair interactions of protons and TS cations with conjugate anions. Mo-POM clusters have a larger covalent component of DPE than W-POM; such covalency is disrupted upon deprotonation but not fully recovered at ion-pair transition states, leading to higher activation energies and lower rates on acids with greater covalency.

■ ASSOCIATED CONTENT

Supporting Information

The following file is available free of charge on the ACS Publications website at DOI: 10.1021/cs501599y.

Supplemental data (solid-state mass NMR, DFT-derived energies, HAE, UV−vis spectra, etc.) and derivations of rate equations and HAE averaging expression (PDF)

■ AUTHOR INFORMATION

Corresponding Author

*E-mail: iglesia@berkeley.edu.

Notes

The authors declare no competing financial interest.

■ ACKNOWLEDGMENTS

This material is based upon work supported by the U.S. Department of Energy, Office of Science, Office of Basic Energy Sciences, under contract no. DE-AC05-76RL0-1830. Computational facilities were provided by the Environmental Molecular Science Laboratory (EMSL) at Pacific Northwest National Laboratory (PNNL), a DOE Office of Science User Facility, under proposal no. 47582. The use of molecular DFT calculations using Gaussian program was made possible by the Extreme Science and Engineering Discovery Environment (XSEDE) and a UC Berkeley College of Chemistry facility, which are supported by National Science Foundation grant numbers (ACI-1053575 and CHE-0840505, respectively). The ^{31}P-MAS NMR measurements were performed at the Caltech Solid State NMR Facility with the assistance of Dr. Sonjong Hwang. We are grateful to Mr. William Knaeble (UC Berkeley) for developing two-dimensional visualizations of the HAE distributions in POM clusters and for technical discussions, Ms. Sarika Goel (UC Berkeley) for TEM imaging, and Mr. Neelay Phadke for a careful review of this manuscript.

■ REFERENCES

(1) Pope, M. T.; Muller, A. *Angew. Chem., Int. Ed.* **1991**, *30*, 34−48.
(2) Okuhara, T.; Mizuno, N.; Misono, M. *Adv. Catal.* **1994**, *41*, 113−252.
(3) Misono, M. *J. Chem. Soc. Chem. Commun.* **2001**, 1141−1152.

DOI: 10.1021/cs501599y
ACS Catal. 2015, 5, 666−682

(4) Song, I. K.; Barteau, M. A. *J. Mol. Catal. A: Chem.* **2004**, *212*, 229−236.
(5) Barteau, M. A.; Lyons, J. E.; Song, I. K. *J. Catal.* **2003**, *216*, 236−245.
(6) Macht, J.; Janik, M. J.; Neurock, M.; Iglesia, E. *Angew. Chem., Int. Ed.* **2007**, *119*, 8010−8014.
(7) Macht, J.; Janik, M. J.; Neurock, M.; Iglesia, E. *J. Am. Chem. Soc.* **2008**, *130*, 10369−10379.
(8) Macht, J.; Carr, R. T.; Iglesia, E. *J. Catal.* **2009**, *264*, 54−66.
(9) Macht, J.; Carr, R. C.; Iglesia, E. *J. Am. Chem. Soc.* **2009**, *131*, 6554−6565.
(10) Carr, R. C.; Neurock, M.; Iglesia, E. *J. Catal.* **2011**, *278*, 78−93.
(11) Tatibouët, J. M. *Appl. Catal. A.: General* **1997**, *148*, 213−252.
(12) Soares, A. P. V.; Portela, M. F.; Kiennemann, A. *Catal. Rev.* **2005**, *47*, 125−174.
(13) Mars, P.; van Krevelen, D. W. *Chem. Eng. Sci.* **1954**, *3*, 41−59.
(14) Brown, G. M.; Noe-Spirlet, M.-R.; Busing, W. R.; Levy, H. A. *Acta Cryst. B* **1977**, *33*, 1038−1046.
(15) Liu, H.; Iglesia, E. *J. Phys. Chem. B* **2003**, *107*, 10840−10847.
(16) Cheung, P.; Liu, H.; Iglesia, E. *J. Phys. Chem. B* **2004**, *108*, 18650−18658.
(17) Kubelka, P.; Munk, F. Z. *Tech. Phys.* **1931**, *12*, 593−601.
(18) Kortüm, G. *Reflectance Spectroscopy*; Springer-Verlag: Berlin, 1969; pp 1−216.
(19) Barton, D. G.; Shtein, M.; Wilson, R. D.; Soled, S. L.; Iglesia, E. *J. Phys. Chem. B* **1999**, *103*, 630−640.
(20) (a) Kresse, G.; Hafner, J. *Phys. Rev. B* **1993**, *47*, 558−561. (b) Kresse, G.; Furthmuller, J. *Comput. Mater. Sci.* **1996**, *6*, 15−50. (c) Kresse, G.; Furthmuller, J. *Phys. Rev. B* **1996**, *54*, 11169−11186.
(21) Perdew, J. P.; Chevary, J. A.; Vosko, S. H.; Jackson, K. A.; Pederson, M. R.; Singh, D. J.; Fiolhais, C. *Phys. Rev. B* **1992**, *46*, 6671−6687.
(22) Kresse, G.; Joubert, D. *Phys. Rev. B* **1999**, *59*, 1758−1775.
(23) Deshlahra, P.; Iglesia, E. *J. Phys. Chem. C* **2014**, *118*, 26115−26129.
(24) Deshlahra, P.; Carr, R. T.; Iglesia, E. *J. Am. Chem. Soc.* **2014**, *136*, 15229−15247.
(25) Vanderbilt, D. *Phys. Rev. B* **1990**, *41*, 7892−7895.
(26) Jacquemin, D.; Perpète, E. A.; Ciofini, I.; Adamo, C. *J. Chem. Theory Comput.* **2010**, *6*, 1532−1537.
(27) Frisch, M. J.; Trucks, G. W.; Schlegel, H. B.; Scuseria, G. E.; Robb, M. A.; Cheeseman, J. R.; Scalmani, G.; Barone, V.; Mennucci, B.; Petersson, G. A.; Nakatsuji, H.; Caricato, M.; Li, X.; Hratchian, H. P.; Izmaylov, A. F.; Bloino, J.; Zheng, G.; Sonnenberg, J. L.; Hada, M.; Ehara, M.; Toyota, K.; Fukuda, R.; Hasegawa, J.; Ishida, M.; Nakajima, T.; Honda, Y.; Kitao, O.; Nakai, H.; Vreven, T.; Montgomery, J. A., Jr.; Peralta, J. E.; Ogliaro, F.; Bearpark, M.; Heyd, J. J.; Brothers, E.; Kudin, K. N.; Staroverov, V. N.; Kobayashi, R.; Normand, J.; Raghavachari, K.; Rendell, A.; Burant, J. C.; Iyengar, S. S.; Tomasi, J.; Cossi, M.; Rega, N.; Millam, M. J.; Klene, M.; Knox, J. E.; Cross, J. B.; Bakken, V.; Adamo, C.; Jaramillo, J.; Gomperts, R.; Stratmann, R. E.; Yazyev, O.; Austin, A. J.; Cammi, R.; Pomelli, C.; Ochterski, J. W.; Martin, R. L.; Morokuma, K.; Zakrzewski, V. G.; Voth, G. A.; Salvador, P.; Dannenberg, J. J.; Dapprich, S.; Daniels, A. D.; Farkas, Ö.; Foresman, J. B.; Ortiz, J. V.; Cioslowski, J.; Fox, D. J. *Gaussian 09*; Gaussian, Inc.: Wallingford, CT, 2009.
(28) (a) Becke, A. D. *J. Chem. Phys.* **1993**, *98*, 5648−5652. (b) Lee, C.; Yang, W.; Parr, R. G. *Phys. Rev. B* **1988**, *37*, 785−789.
(29) Pettersson, L.; Andersson, I.; Öhman, L.-O. *Inorg. Chem.* **1986**, *25*, 4726−4733.
(30) Hu, J.; Burns, R. C.; Guerbois, J.-P. *J. Mol. Catal. A* **2000**, *152*, 141−155.
(31) Grinenval, E.; Rozanska, X.; Baudouin, A.; Berrier, E.; Delbecq, F.; Sautet, P.; Basset, J.-M.; Lefebvre, F. *J. Phys. Chem. C* **2010**, *114*, 19024−19034.
(32) Massart, R.; Contant, R.; Fruchart, J.-M.; Ciabrini, J.-P.; Fournier, M. *Inorg. Chem.* **1977**, *16*, 2916−2921.
(33) (a) Soled, S. L.; Mcvicker, G. B.; Murrell, L. L.; Sherman, L. G.; Dispenziere, N. C., Jr.; Hsu, S. L.; Waldman, D. *J. Catal.* **1988**, *111*, 286−295. (b) Baertsch, C. D.; Komala, K. T.; Chua, Y. H.; Iglesia, E. *J. Catal.* **2002**, *205*, 44−57.
(34) Fournier, M.; Feumi-Jantou, C.; Rabia, C.; Hervé, G.; Launay, S. *J. Mat Chem.* **1992**, *2*, 971−978.
(35) Liu, H.; Iglesia, E. *Angew. Chem., Int. Ed.* **2003**, *42*, 5072−5075.
(36) (a) Zhang, W.; Desikan, A.; Oyama, S. T. *J. Phys. Chem.* **1995**, *99*, 14468−14476. (b) Zhang, W.; Oyama, S. T. *J. Phys. Chem.* **1996**, *100*, 10759−10767.
(37) Seman, M.; Kondo, J. N.; Domen, K.; Radhakrishnan, R.; Oyama, S. T. *J. Phys. Chem. B* **2002**, *106*, 12965−12977.
(38) Kilos, B.; Bell, A. T.; Iglesia, E. *J. Phys. Chem. C* **2009**, *113*, 2830−2836.
(39) Liu, H.; Iglesia, E. *J. Phys. Chem. B* **2005**, *109*, 2155−2163.
(40) Goodrow, A.; Bell, A. T. *J. Phys. Chem. C* **2007**, *111*, 14753−14761.
(41) Weber, R. S. *J. Phys. Chem.* **1994**, *98*, 2999−3005.
(42) Argyle, M. D.; Chen, K.; Resini, C.; Krebs, C.; Bell, A. T.; Iglesia, E. *J. Phys. Chem. B* **2004**, *108*, 2345−2353.
(43) Dreuw, A.; Weisman, J. L.; Head-Gordon, M. *J. Chem. Phys.* **2003**, *119*, 2943−2946.
(44) Horbatenko, Y.; Vyboishchikov, S. F. *ChemPhysChem* **2011**, *12*, 1118−1129.
(45) Ichikawa, M. *Acta Crystallogr.* **1978**, *B34*, 2074−2080.
(46) Proft, F. D.; Langenaeker, W.; Geerlings, P. *Tetrahedron* **1995**, *51*, 4021−4032.
(47) Bader, R. *Acc. Chem. Res.* **1985**, *18*, 9−15.
(48) (a) Henkelman, G.; Arnaldsson, A.; Jónsson, H. *Comput. Mater. Sci.* **2006**, *36*, 354−360. (b) Sanville, E.; Kenny, S. D.; Smith, R.; Henkelman, G. *J. Comput. Chem.* **2007**, *28*, 899−908.
(49) Gussi, B. *Phys. Scr.* **2004**, *T109*, 141−151.
(50) Dvorak, M.; Wei, S.; Wu, Z. *Phys. Rev. Lett.* **2013**, *110*, 016402.

DOI: 10.1021/cs501599y
ACS Catal. 2015, 5, 666−682